Brodogradnja Volume 77 Number 3 (2026) 77314

journal homepage: www.brodogradnja.fsb.hr

Brodogradnja

An International Journal of Naval Architecture and Ocean Engineering for Research and Development

University of Zagreb Faculty of Mechanical Engineering and Naval Architecture

Numerical analysis of bow flow characteristics on a research vessel under drift and turning conditions

Tiecheng Wu[1,2,3], *CanCan He*[1], *Yuanjie Yang*[1], *Zhengren Wang*[1], *Wanzhen Luo*[1,2,3,*], *Weitao Cao*[1]

[1] *School of Ocean Engineering and Technology, Sun Yat-sen University & Southern Marine Science and Engineering Guangdong Laboratory (Zhuhai), Zhuhai, 519000, China*
[2] *Guangdong Provincial Key Laboratory of Information Technology for Deep Water Acoustics，Zhuhai, 519082, China*
[3] *Zhuhai Research Center，Hanjiang National Laboratory，Zhuhai, 519082, China*

ARTICLE INFO

Keywords:
Scientific research vessel
Drift angles
Turning motion
Flow field around bow
CFD

ABSTRACT

This study employs numerical simulations to analyse the flow field characteristics around the bow of a research vessel under drift angles of 0°, 10°, and 20°, as well as during turning motions. The investigation focuses on how different operating conditions influence the velocity, pressure, streamline distribution, and vortex structures. Results indicate that an increase in drift angle leads to more complex flow patterns and vortex evolution, which consequently intensifies hull rolling and turbulence, thereby affecting navigation stability. Variations in pressure gradients alter the streamline distribution along the hull surface, modifying ship forces and the surrounding flow, and contributing to bubble sweep-down near the bow. During turning motion, the flow field evolves through four sequential stages—straight sailing, yawing, deceleration, and steady rotation—each corresponding to distinct ship motion states and exhibiting clear stage-dependent changes in flow structure and hydrodynamic performance. The identified flow mechanisms, particularly the strong downwash and vortex dynamics under high drift angles, provide critical insights for assessing and mitigating acoustic interference risks for research vessels during complex manoeuvring operations.

1. Introduction

Scientific research vessels encounter unique challenges from bow wake-induced bubbles affecting multi-beam acoustic equipment. This interference is particularly pronounced during oblique sailing and turning manoeuvres, which are essential yet problematic phases in survey operations. The underlying mechanism lies in the complex bow flow, where vortical structures and pressure fields directly govern the entrainment, transport, and accumulation of bubbles towards the hull-mounted transducers. Therefore, a detailed analysis of the governing flow field characteristics—especially the vortex dynamics, pressure distribution, and velocity fields—is fundamental to diagnosing and mitigating bubble interference. To tackle such complex hydrodynamic problems, Computational Fluid Dynamics (CFD) serves as a powerful and well-established tool for resolving the intricate flow physics around a ship's hull, as evidenced by its

* Corresponding author.
E-mail address: luowzh5@mail.sysu.edu.cn

https://doi.org/10.21278/brod77314
Received 26 December 2026; Received in revised form 9 February 2026; Accepted 14 February 2026
Available online 27 February 2026
ISSN 0007-215X; eISSN 1845-5859

successful application in studies of viscous roll damping [1], wave-added resistance [2], and wake characterisation [3].

The predictive fidelity of CFD must be validated against benchmark tests. In ship hydrodynamics, the core benchmarks are the static drift test and the dynamic turning test. The static drift test simulates oblique sailing at a fixed drift angle, leading to a strongly asymmetric pressure distribution—high pressure on the windward side and low pressure on the leeward side. This pressure difference generates the dominant lateral force and yaw moment, and fundamentally alters the bow vortex structures, setting the stage for asymmetric bubble transport. Dynamic turning tests simulate more realistic manoeuvring. The hydrodynamic coefficients obtained are fundamental for building ship manoeuvring mathematical models (e.g., the MMG model). These models bridge fundamental research and engineering practice, enabling: (a) Assessment of manoeuvring safety (e.g., predicting turning diameter); (b) Development of automated control systems (e.g., autopilots); (c) Optimization of hull forms. Thus, studies employing BEM, CFD, or experiments ultimately contribute by refining these crucial coefficients and deepening the understanding of the underlying flow physics, thereby enhancing the reliability and safety of engineering tools.

Bubble interference originates from the bow flow, where bubbles are primarily generated through bow wave breaking—a process involving complex air entrainment and vortical structures [4]. Critically, as established above, the subsequent transport and accumulation of these bubbles are governed by the macroscopic vortical structures and pressure fields around the bow. The ship's drift angle is the paramount operational parameter that drastically reshapes these very flow features. Thus, understanding drift angle's impact on these bubble-governing vortex dynamics is essential. Research shows drift angle significantly affects flow: Longo and Stern [5] found significant changes in wave amplitudes and wake asymmetry around container ships. Tanaka et al. [6] noted complex flow fields and reduced manoeuvrability due to vortex shedding at large drift angles. Pinto et al. [7] observed that vortices grow stronger and more complex at extreme drift angles, causing flow instability. Bhushan et al. [8] analysed attitude changes in a ship model at drift angles of 0 and 20 degrees. Liu et al. [9] reported stronger flow separation and increased lateral forces and yaw moments at higher drift angles. Hosseini et al. [10] employed DES to reveal strong asymmetric vorticity and pressure fields on a planing hull at drift angles up to 20°.

Zhang et al. [11] investigated drift angles' effects on KCS ship dynamics. Okuda et al. [12] demonstrated the practical accuracy of a simulation method based on captive model test data for predicting manoeuvring motions at large drift angles for a ship with a flapped rudder. Ma et al. [13] reported that bank proximity in confined waters induces asymmetric hull forces and a lateral shift in the stern wake. Zhang et al. [14] investigated the effects of bow configurations on flow fields around the bow. Wu et al. [15] analysed the DTMB5415 bow flow field under various trim conditions, focusing on wave profiles and vorticity. Capone et al. [16] used SPIV to reveal asymmetric wake patterns in a twin-propeller ship. Broglia et al. [17] evaluated CFD predictions for the Delft catamaran, noting impacts of grid resolution and turbulence models. Li et al. [18] studied bubbly wake formation in the Athena R/V, analysing bubble dynamics. Lee et al. [19] discussed the impact of drift angle on stability in shallow water. Roychoudhury et al. [20] simulated KVLCC2 manoeuvring in different water depths, observing significant force and moment influences. Kramer et al. [21] tested hull forms at different drift angles and Froude numbers, comparing results with lift models. Meng and Wan [22] employed overset mesh technology to investigate the viscous flow around the obliquely towed KVLCC2M model. This study serves as a well-established benchmark for applying overset methods to ship manoeuvring flow simulations. Further demonstrating the robustness of this approach for free-running conditions, Kim et al. [23] successfully utilized an overset mesh system within a CFD framework to conduct virtual free-running turning tests for the KVLCC2 tanker in both calm water and waves, obtaining results in good agreement with experimental data. Abbas et al. [24] studied unsteady wake and propeller load with different turbulence models. Fureby et al. [25] compared flow field characteristics using various turbulence models. Abdel et al. [26] studied KVLCC2 flow patterns using CFD and various turbulence models. Zhou et al. [27] assessed hydrodynamic interference in large container ships, finding accurate predictions at small drift angles. Xing et al. [28] analysed vortex structures at different drift angles. Kim et al. [29] developed a RANS solver for tankers with different stern shapes, validating simulations

against experimental data. Furthermore, efficient potential-flow methods and panel codes continue to provide valuable benchmark data and global insights into drift forces, coupled motions, and depth effects [30, 31].

Research on flow field characteristics around the bow during oblique navigation is limited. While potential-flow analyses offer valuable benchmarks, a detailed understanding of the evolving vortex structures and their direct link to bubble sweep-down phenomena under these conditions is scarce. This area is crucial because bubble sweep down, affecting acoustic equipment, arises from bow flow dynamics. For bubble dynamics modelling, advanced numerical approaches exist [32]. The present study focuses on a surface research vessel to explore bow flow characteristics and bubble sweep-down potential. The increase in drift angle significantly affects the vortex structures around the ship's bow, which in turn has an important impact on the vessel's stability and manoeuvrability. By studying complex vortex structures, key areas of flow separation and vortex generation can be identified, thereby guiding ship design. Studying this flow field under oblique and turning conditions can help address these issues in future scientific vessels.

Recent advances enable exploration of wave-breaking microscopic mechanisms [33]. However, linking these microscopic multiphase flow mechanisms to the macroscopic flow field around a practical research vessel during dynamic manoeuvres remains lacking.

While extreme drift angles (e.g., 20°) are uncommon during steady course-keeping, they are highly relevant for dynamic manoeuvring phases, such as the initiation of a sharp turn, station-keeping in cross-currents, or recovery from adverse conditions. Although potential-flow methods and RANS studies provide valuable global force data, a detailed understanding of the evolution of fine-scale bow flow structures (e.g., vortices, downwash) of a research vessel hull form under large static drift angles and throughout a dynamic turning process remains scarce. The direct link between these evolving macroscopic flow features and the potential for bubble sweep-down is also not well quantified. The primary aims of this study are: (1) To establish and validate a high-fidelity CFD framework for ship manoeuvring flows. (2) To investigate the influence of static drift angle (0°, 10°, 20°) on the bow flow field. (3) To analyse the phase evolution of the bow flow field during a steady turning manoeuvre. (4) To discuss the implications of the identified flow phenomena on the potential for acoustic equipment interference.

This paper covers the following: Section 2 introduces the hull geometry, Section 3 details the numerical methods, including governing equations and turbulence models, computational domain, and mesh. Section 4 discusses numerical validation. Section 5 presents and analyses the flow field characteristics under different navigation conditions. Section 6 concludes the paper.

2. Geometric model

The benchmark model DTMB5512 [34, 35] and the Model SYSU are selected as the research objects in this paper. The Model SYSU measures a total length of 3.412 m and a width of 0.579 m. The DTMB5512 model has a length between perpendiculars of 3.048 m and a width of 0.409 m. The DTMB5512 used for the calculation is shown in Figure 1(a) and Model SYSU is in Figure 1(b). The coordinate system's origin is at the centre of gravity. The X-axis runs parallel to the hull's centreline from bow to stern, the Y-axis extends from port to starboard, and the Z-axis points vertically upward toward the free surface.

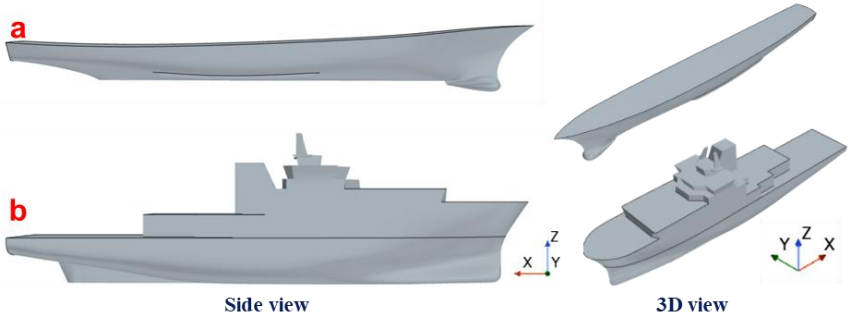

Fig. 1 Geometric model: (a) DTMB 5512; (b) Model SYSU.

3. Numerical simulation method

3.1 Governing equations

The numerical model is established to simulate the flow around a surface ship advancing in calm water. The physical problem is conceptualized within a three-dimensional computational domain representing a virtual towing tank. This domain contains two immiscible, viscous fluids: water below and air above, separated by a deformable interface—the free surface. The core assumptions underpinning the mathematical model are: (1) both fluids are incompressible; (2) the flow is isothermal, and heat transfer is neglected; (3) surface tension effects are considered negligible for the macroscopic flow phenomena under study.

Numerical simulations of the flow field around a ship's bow using CFD techniques require adherence to three fundamental equations: the continuity, momentum, and energy equations. In this study, the fluid is treated as incompressible, and thermal effects are excluded. Therefore, energy conservation is inherently satisfied, enabling us to focus exclusively on solving the continuity and momentum equations.

Continuous equations:

$$\frac{\partial u_i}{\partial x_i} = 0 \tag{1}$$

Momentum equation:

$$\frac{\partial u_i}{\partial t} + \frac{\partial}{\partial x_j}(u_i u_j) = -\frac{1}{\rho}\frac{\partial p}{\partial x_i} + \upsilon \frac{\partial}{\partial x_j}\left(\frac{\partial u_i}{\partial x_j} + \frac{\partial u_j}{\partial x_i}\right) + \frac{\partial}{\partial x_j}\left(-\overline{u_i' u_j'}\right) \tag{2}$$

where u_i is the average velocity, x_i is the coordinates, t is the time, ρ is the fluid density, p is the average time pressure, υ is the viscosity coefficient of fluid motion, and $-\rho\overline{u_i' u_j'}$ is the Reynolds stress tensor.

3.2 Turbulence model and free surface treatment method

Additional to accurately captures the vortex structures in the flow field around the bow area, the SST *k-ω* Detached Eddy Simulation (DES) method was employed for numerical analysis. DES is better suited for handling flows with complex geometries, effectively capturing important details in the flow field and accurately simulating both large-scale and small-scale vortices. The DES approach leverages the Reynolds-Averaged Navier-Stokes (RANS) simulation to resolve the boundary layer and employs Large Eddy Simulation (LES) to handle the unsteady separated flow regions, thereby combining the strengths of both techniques. The mathematical formulation of the SST *k-ω* turbulence model is as follows [36]:

$$\frac{\partial}{\partial t}(\rho k) + \frac{\partial}{\partial x_i}(\rho k u_i) = \frac{\partial}{\partial x_j}\left(\Gamma_k \frac{\partial k}{\partial x_j}\right) + G_k - Y_k + S_k \tag{3}$$

where the u_i is the turbulent viscosity, and the Γ_k represent the effective diffusivity of k respectively; G_k is the turbulent kinetic energy due to the average velocity gradient; Y_k represent the dissipation of turbulent currents k.

The free surface of the numerical tank was modelled using the two-phase volume-of-fluid (VOF) method [37]. with the high-resolution interface capturing (HRIC) scheme [38]. In the VOF model, all phases share a single set of momentum equations, and the interface is reconstructed by solving a transport equation for the volume fraction α_i of one phase within each computational cell. The transport equation is given as:

$$\frac{\partial \alpha_i}{\partial t} + \nabla \cdot [(u_i - u_g)\alpha_i] + \nabla \cdot [u_r(1-\alpha_i)\alpha_i] = 0 \tag{4}$$

In this equation, u_i is the velocity field, u_g is the grid velocity, and u_r is a relative velocity term. The volume fraction α_i represents the fractional volume of a cell occupied by the liquid phase, ranging from 0 (gas only) to 1 (liquid only). Based on α_i, the mixture density (ρ) and dynamic viscosity (μ) in each cell are calculated as weighted averages:

$$\rho = \alpha_i \rho_i + (1-\alpha_i)\rho_g \tag{5}$$

$$\mu = \alpha_i \mu_i + (1-\alpha_i)\mu_g \tag{6}$$

To manage boundary wave reflections, which typically affect the main Kelvin wave system, the Euler-overlay method (EOM) [39] was employed to mitigate these reflections effectively.

3.3 Computational domains and boundary conditions

To accurately capture the free surface and wake of the ship model during oblique and turning motions, the entire ship is included within the computational domain. The computational domain, depicted in Figure 2(a), is a large rectangular box representing a towing tank. The ship is positioned with its midship at the origin of the coordinate system. The domain extents are defined relative to the midship: the inlet boundary is located 2.0 *Lpp* upstream of midship, and the outlet boundary is 4.0 *Lpp* downstream of midship. The total width of the domain is 3.0 *Lpp*. The vertical extent of the domain measures 1.7 *Lpp* in total height. This size ensures that boundary effects on the near-hull flow are negligible.

Figure 2(b) is the setup of drift angles. To mitigate the impact of wall effects on the simulation, the inlet, side, outlet, and bottom boundaries of the domain are set as velocity inlets, with the inlet velocity matching the speed of the ship model. The top boundary is configured as a pressure outlet. Additionally, the VOF method described in Section 2.2, using the Euler-overlay method for forcing waves, is employed to establish the free surface and minimize wave reflection at the boundaries. The ship model's surface is treated as a no-slip, impermeable boundary condition. The drift angle, denoted by α, indicates rotation towards the starboard side. In this study, α is set to 0°, 10°, and 20°.

The finite volume method is employed to solve the governing equations. The spatial discretization of the convection terms in the momentum and turbulence equations uses a second-order upwind scheme. For the volume fraction equation, the High-Resolution Interface Capturing (HRIC) scheme is applied to preserve the sharpness of the air-water interface. Gradients are computed using the cell-based least squares method. The pressure-velocity coupling is achieved through the SIMPLE algorithm. The temporal discretization uses a second-order implicit scheme, and the resulting linear systems are solved with an algebraic multigrid solver. A fixed physical time step of 0.01 s is used for all transient simulations, ensuring the maximum Courant number remains below 1.0 in the refined flow regions for stability and accuracy.

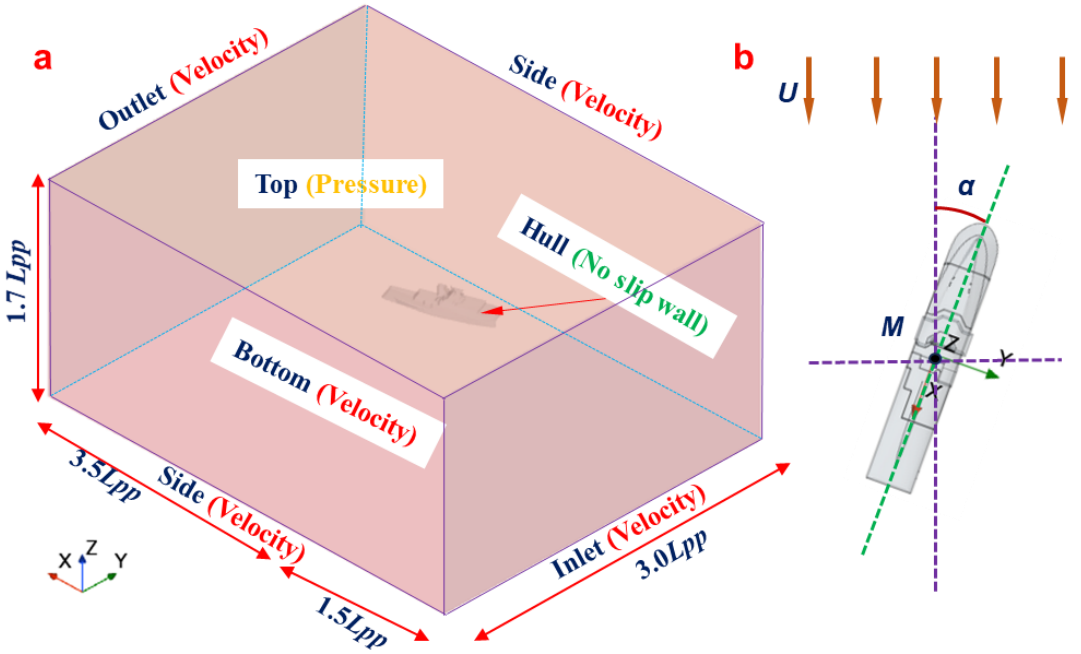

Fig. 2 Computational domain (a) and (b) Setup of drift angles.

3.4 Meshing

The discretization grid is created using STAR-CCM+'s automatic unstructured hexahedral grid generator. The Surface Remesher module first processes the hull to generate a high-quality surface mesh, which is then used to construct a trimmed mesh. Mesh refinement focuses on the Kelvin wave region, free surface, and areas near the hull to capture flow details accurately. Figure 3 shows the mesh refinement. A prism layer mesh, consisting of 15 layers with a total thickness of 0.015 m, is applied to the hull to resolve flow dynamics, keeping $y+$ values below 1. The base mesh size is 0.01 m, and the final grid count is 41 million.

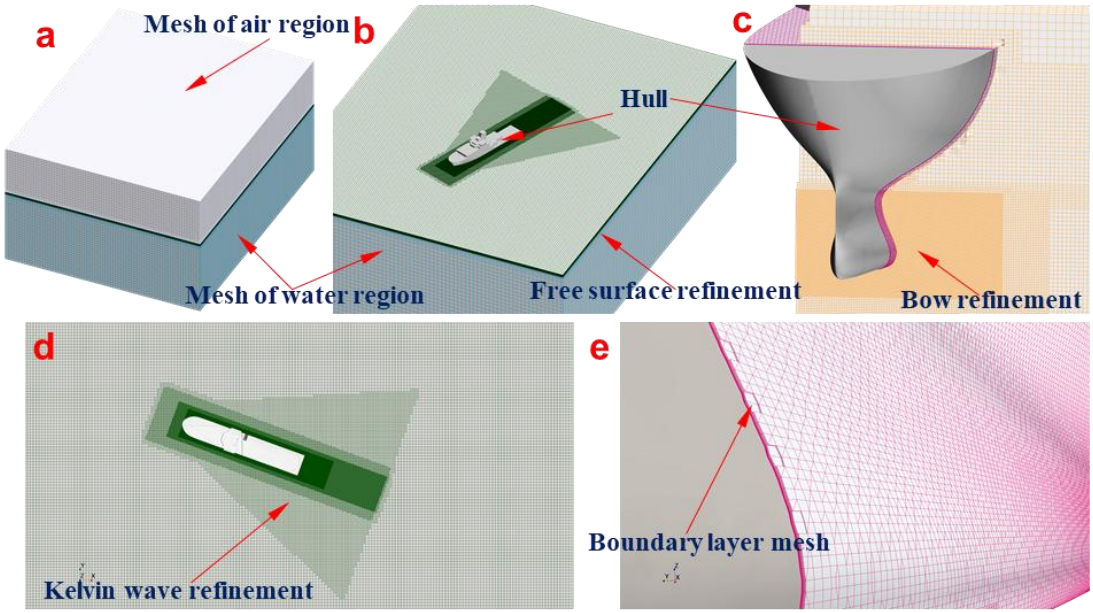

Fig. 3 Mesh refinement of the computational domain: (a) Overall view of the mesh; (b) Mesh around the hull; (c) Bow refinement of the mesh; (d) Kelvin wave refinement of the mesh; and (e) Boundary layer around the hull.

3.5 Motion Simulation Setup

The hydrodynamic analysis is conducted for two types of conditions: static (fixed) drift and dynamic turning. In the static drift cases, the ship's position and attitude are completely fixed at prescribed drift angles (α = 0°, 10°, 20°). All six degrees of freedom (DOF) are constrained. This approach allows for a systematic investigation of the isolated effect of drift angle on the developed flow field, forces, and vortex structures.

The turning motion of the ship is a situation in which the drift angle of the oblique navigation is constantly changing. The ship was free to move in surge, sway, and yaw. At the same time, the flow field near the ship undergoes complex changes. The simulation starts from a steady straight-ahead condition ($\alpha = 0°$). A constant external yaw moment is applied to the hull, emulating the effect of a fixed rudder deflection, which initiates and sustains the turning motion. The resultant coupled motion of the ship is governed by the 3-DOF rigid-body equations of motion in the horizontal plane:

$$(m+m_x)\dot{u}-(m+m_y)\dot{v}r = X \tag{7}$$

$$(m+m_y)\dot{v}+(m+m_x)\dot{u}r = Y \tag{8}$$

$$(I_{zz}+J_{zz})\dot{r}+mx_G(\dot{v}+ur) = N \tag{9}$$

where m is the ship mass; I_{zz} is the moment of inertia about the z-axis; m_x, m_y, J_{zz} are the added mass/inertia coefficients; u, v, r are surge velocity, sway velocity, and yaw rate, respectively; X, Y, N are the fluid dynamic forces and moment acting on the hull.

The overset (chimera) mesh technique was employed to accommodate the large rotational displacement. The coupling between the fluid dynamics (providing X, Y, N) and the rigid-body motion (updating the ship's position and velocity) is handled by the Dynamic Fluid Body Interaction (DFBI) module [40]. The DFBI module, which establishes the coupling relationship between fluid and rigid body interactions and enables the simulation of rigid body motion in response to fluid pressure, shear forces, and user-defined external forces, is used to calculate the rotational motion of the ship model, and the computational domain moves with the ship.

4. Verification

4.1 Meshing sensitivity analysis

Grid division within the calculation domain significantly impacts computation accuracy. According to Li et al. [41], a finer grid resolution increases the precision of capturing complex flow features, such as turbulence and boundary layer separation, leading to more accurate results. However, excessive refinement can result in higher computational costs without proportional gains in accuracy, especially when diminishing returns are observed in areas of minimal flow variation. Additionally, adaptive grid refinement techniques are often employed to balance accuracy and computational efficiency, focusing higher resolution grids in regions with steep gradients or high flow complexity; see Wang et al. [42, 43]. This study investigates the influence of meshing on calculation results, emphasizing the importance of mesh refinement for convergence. A critical factor in achieving convergence is determining the mesh refinement ratio, r. For effective convergence, r should be maintained below 1.5. The formula for calculating r is given by:

$$r = \left(\frac{N}{N^*}\right)^{\frac{1}{d}} \tag{4}$$

where N is the number of fine grids, which can also be regarded as the number of finer grids in the adjacent grid setup, N^* is the number of medium grids and can also be regarded as the number of coarser grids in the adjacent grid setup, and d is the number of dimensions. In this validation, the dimension $d = 3$.

The numerical calculation of the total drag coefficient *Ct* and the free surface under the condition of *Fr* = 0.28 were selected to verify the grid independence. By adjusting the base size set during meshing, three sets of meshes with different threes of density are generated. The calculated results of the *Ct* under three different dense grids are compared with the experimental values [34, 35] under the same working conditions, and the results are shown in Table 1. The error between the calculated results and the experimental values of the three grids with different densities is within 3 %. So, it can be assumed that there is a good agreement between simulation and experiment. Figure 4(a) is the free surface calculated using the three different meshes when *Fr* = 0.28. It shows that the free surface shapes from three meshes with different densities are similar, indicating minimal mesh dependence and confirming mesh independence.

Table 1 Comparison of *Ct* with experimental values under three grids.

	Experimental values	Coarse	Medium	Fine
Cell number	/	2223342	3757103	6524824
Ct	0.004607	0.004734	0.004639	0.004510
Relative error/%	/	2.757 %	0.695 %	-2.105 %

4.2 Time step sensitivity analysis

To verify time-step independence, the numerical calculation of the total drag coefficient *Ct* and the free surface waveform under the condition of *Fr* = 0.28, comparing these with experimental values were investigated. In this analysis, three different time steps 0.005 s, 0.01 s, and 0.02 s were selected. Calculations were performed using the medium-density grid from the previous section. The results obtained were compared with the experimental values [34, 35] and are presented in Table 2. The comparison reveals that the calculated *Ct* values at the three different time steps show strong consistency with the experimental values, with discrepancies all within 5 %. This indicates that the chosen time steps do not significantly affect the accuracy of the results and confirms the time-step independence of the numerical calculations. Similarly, Figure 4(b) illustrates the shape of the free surface calculated using the three different time steps when *Fr* = 0.28. The minimal differences observed among the three cases indicate that the model exhibits little dependence on the chosen time step.

Table 2 Comparison of *Ct* with the experimental value at three-time steps.

Time-step	*Ct*	Relative error/%
0.005s	0.004726	2.583 %
0.01s	0.004639	0.695 %
0.02s	0.004397	-4.558 %
EFD	0.004607	-

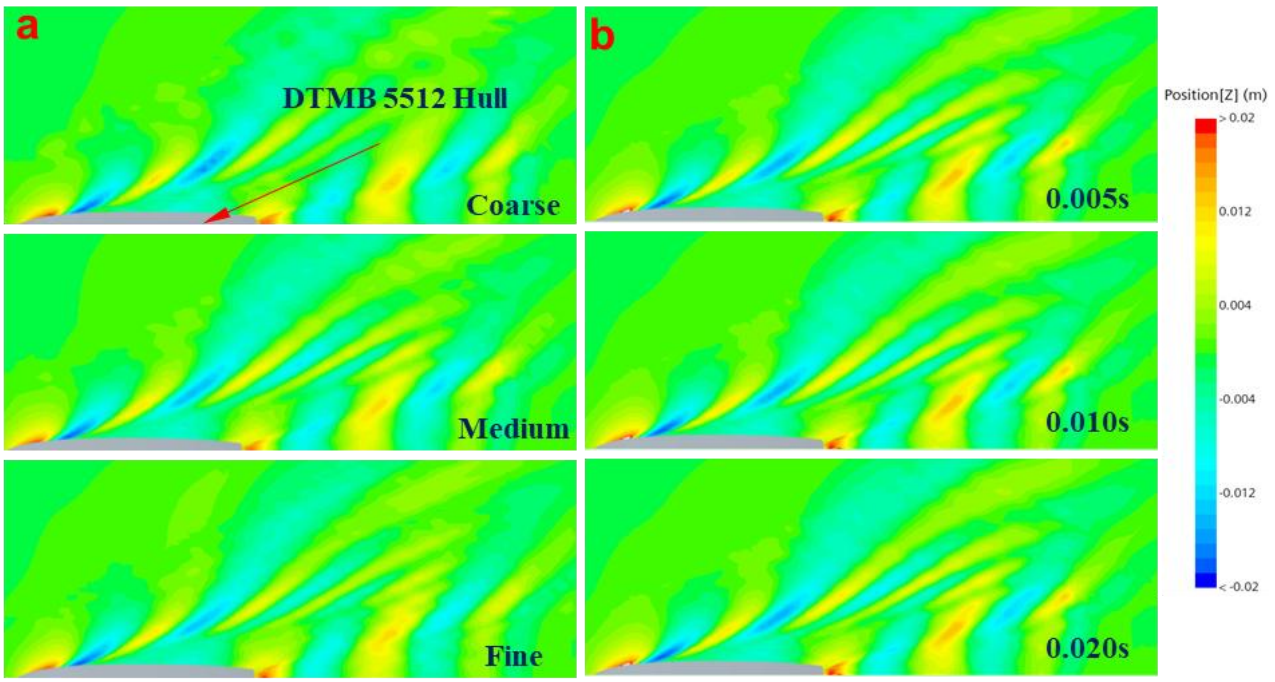

Fig. 4 Comparison of free surface elevation contours (a) Three different meshes; (b) Three different time steps

4.3 Validation of the numerical model

The IIHR towing tank (Iowa Institute of Hydraulic Research, University of Iowa) has conducted a detailed study of the DTMB5512 ship model, with detailed public test data [34, 35]. In this subsection, the resistance, free surface waveform and flow field, and eddy structure distribution of the DTMB5512 under fixed attitude conditions are simulated and predicted, and the correctness of the numerical model is verified by using the experimental data of the IIHR towing tank [44]. A tiered validation strategy was employed, where the choice of turbulence model and mesh resolution was aligned with the specific objective of each phase.

In the case of a drift angle of 0°, the primary goal was to efficiently validate the resistance coefficient and free-surface waveform. Therefore, simulations were performed using the SST k-ω RANS turbulence model. Leveraging symmetry, a half-ship model of the DTMB was utilized. The total resistance coefficient Ct and the free surface flow field of the DTMB5512 at Fr = 0.28 were compared with numerical simulation results under corresponding working conditions. A medium number of grids and a time step of 0.01 s were used for the calculations. The experimental value of Ct was 0.004607, while the numerical result was 0.004639, yielding a relative error of 0.695 %. When Fr=0.28, the relative error between the numerical results of the total resistance coefficient Ct obtained by this method and the experimental values remained within 2 %. Figures 5(a) and 5(b) show the free surface elevation contours of DTMB 5512 hull at Fr = 0.28 for the model test and numerical calculations, respectively. Consistency in waveforms demonstrates the correctness of the numerical method, as it indicates that the numerical calculations accurately replicate the actual phenomena observed in the experiments.

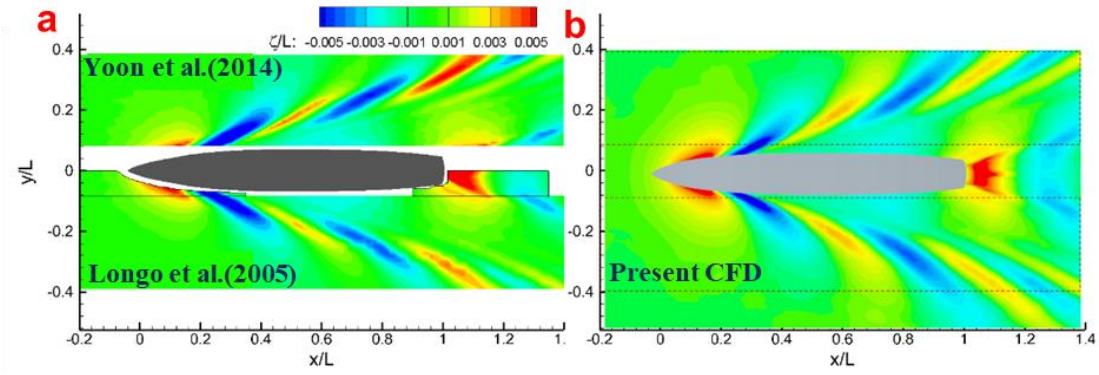

Fig. 5 Free surface elevation contours of DTMB 5512 hull at Fr = 0.28 obtained from: (a) EFD data from Yoon and Longo's experiment; (b) Present CFD

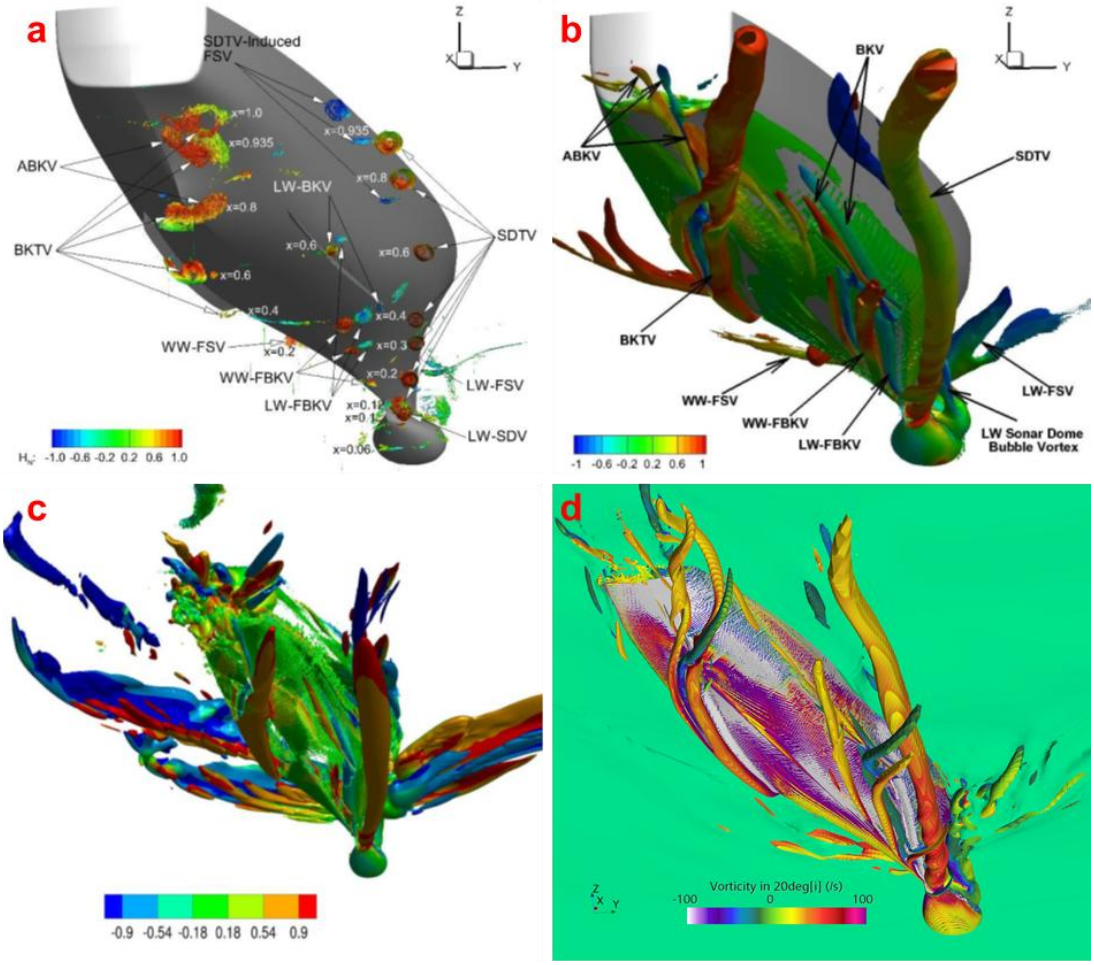

Fig. 6 Comparison of vortex structures at the bottom: (a) EFD data from IIHR's experiment; (b) CFD Ship-IOWA (DES 84M); (c) NavyFOAM (RANS, 68M); (d) Present CFD

To validate the feasibility of the CFD method presented in this paper, a comparison of the vortex structures at a drift angle of 20° was conducted. For this case, a full-scale simulation of the DTMB 5415 was performed. A locally refined mesh targeting the anticipated separation regions was employed, resulting in a total of approximately 32 million cells. This resolution ensures the DES model is adequately activated to capture the dominant vorticial structures for qualitative comparison. Figure 6 shows the comparison of vortex structures at the bottom. Figure 6(a) is the EFD vortex structures data from IIHR's experiment. Figure 6(b) is the CFD Ship-IOWA vortex structures with DES method. Figure 6(c) is the NavyFOAM vortex structures with RANS method and Figure 6(d) is the vortex structures of Present CFD. At Q = 120 s^2

(Q is defined by [45]), the proposed method distinctly captures the sonar dome tip vortices (SDTV) and bilge keel tip vortices (BKTV), along with several small vortices around the bow. The simulation also effectively represents the windward free surface vortices (WW-FSV), fore-body keel vortices (WW-FBKV), leeward fore-body keel vortices (LW-FBKV), and mid-hull vortex (MHV). However, there are some discrepancies in the after-body keel vortex (ABKV), particularly in the development direction of the vortex. Additionally, the windward shoulder-free surface vortices (WW-Shoulder-FSV) are not observed in the simulation results, mainly due to differences in the mesh refinement area. The numerical calculations in this paper are consistent with the model test results in terms of the position and strength of the vortex structures, indicating that the numerical method can accurately capture the vortex features. The agreement between the numerical calculations and the features in the experimental results demonstrates the accuracy of the physical representation of the numerical model.

5. Results and discussion

In this section, the flow field results of the bow of the Model SYSU under different working conditions are analysed and discussed in detail. The impact on the velocity field, pressure field, streamline distribution, and vortex structure on both sides of the bow is investigated at drift angles 0°, 10°, 20° and turning motion condition.

5.1 Flow field characteristics of bow area under steady drift angle

The analyses presented in this subsection are based on simulations where the ship's attitude (heave, pitch, and roll) is fixed. This static drift approach is a well-established method to isolate the fundamental effects of the drift angle on the bow flow field, without the confounding interactions introduced by coupled hull motions. It provides a clear baseline understanding of the flow asymmetry, vortex generation, and pressure redistribution driven solely by oblique inflow. We acknowledge that in a real manoeuvring scenario, especially at high drift angles, significant hull motions (notably roll) would occur. These motions would likely modify, and potentially amplify, the flow asymmetries and vortex dynamics described herein. For instance, roll motion could further intensify the leeward-side downwash and alter the lateral pressure distribution, thereby enhancing the risk of bubble entrainment and sweep-down. However, the primary trends and physical mechanisms revealed under static conditions, such as the development of leeward-side downwash, the strengthening and migration of bilge vortices, and the overall loss of symmetry, are expected to form the foundational hydrodynamic response upon which the effects of dynamic ship motions are superimposed. Therefore, the present static-drift results serve as an essential reference for future studies that incorporate coupled ship motions (e.g., free roll, heave, and pitch) to more accurately simulate realistic manoeuvring conditions.

5.1.1 Free surface

Figure 7 presents the free surface waveforms of Model SYSU at varying drift angles. To accurately depict the amplitude and shape of the wave surface near the hull, a bottom view of the ship towards the free surface is adopted in the figure, with the top representing the port side and the bottom representing the starboard. The relative height of the free surface Z/Lpp is dimensionless. At a drift angle of 0°, three peaks and two troughs can be observed within the length of the ship. The peaks and troughs near the bow are prominent, while the stern forms a typical Kelvin wave system. At a drift angle of 10°, the wave peaks at the bow become asymmetric, and the troughs on both sides of the hull connect into one, reducing the peak area. When the drift angle increases to 20°, more severe flow field disturbance is evident, leading to increased wave-making resistance. Water accumulates and rolls near the bow, resulting in the formation of a crest area across the bow on the starboard side. The wave-making on the port side intensifies, and the peak of the trough undergoes a sharp change, indicating a more significant vertical flow near the hull.

The asymmetry and wave-making of at a drift angle 20° are notably increased compared to that at a drift angle 0°. The observed wave patterns belong to the Kelvin wake system, comprising divergent and transverse waves. Under straight-ahead conditions (Figure 7a), these wave components exhibit classical

symmetric distribution. As the drift angle increases, this symmetry is broken. The divergent waves on the windward (starboard) side are compressed and steepened due to the effective increase in local incidence angle, while on the leeward (port) side, they are elongated and attenuated. Concurrently, the transverse wave system near the stern is skewed, and its amplitude becomes asymmetric. This differential modulation of the wave components directly contributes to the increase in wave-making resistance, as quantified in the following section.

The pronounced free-surface asymmetry and water accumulation observed at the drift angle 20° highlight the critical role of large drift angles in triggering and intensifying nonlinear flow dynamics around a ship's bow. While the geometrical complexity of the present three-dimensional curved bow differs significantly from the simplified wedge shape studied by Shao et al. [4], the enhanced disturbances at high drift/yaw angles represent a common hydrodynamic driver for nonlinear free-surface phenomena. The complex waveforms and surface elevations observed in this study can therefore be interpreted as the macroscopic manifestation of an intensified, nonlinear free-surface interaction process that is primarily excited by the large drift angle on the present hull form.

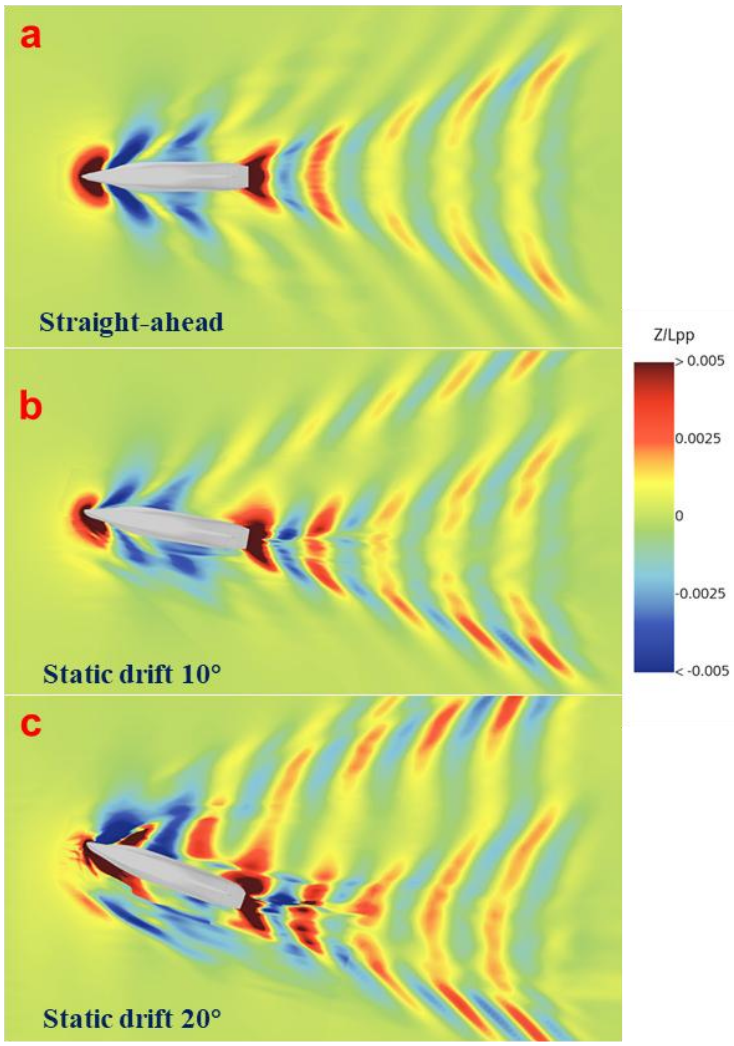

Fig. 7 Free surface elevation contours around SYSU hull under: (a) straight-ahead; (b) static drift of 10-degree and static drift of 20-degree conditions.

Different drift angles alter the direction of wave propagation affecting the free surface wave pattern around the hull. At larger drift angles, the direction of wave propagation may form a larger angle with the disturbance direction caused by the hull, leading to a more complex free surface wave pattern. At smaller drift angles, the waves at the bow and stern of the hull are generally more symmetrical, with a smoother

wave pattern. The free surface waves are more symmetrical and orderly. At larger drift angles, the asymmetry of the free surface waves increases. One side of the hull (the windward side) may exhibit higher wave peaks and stronger fluctuations, while the other side (the leeward side) may remain relatively stable.

5.1.2 Resistance

Table 3 presents the resistance and total resistance characteristics of Model SYSU along the X-axis (length) and Y-axis (beam) at various drift angles. Due to the asymmetry of the hull superstructure during direct navigation, air resistance in the Y-axis direction is negligible. At α = 20°, the total drag is 2.85 times that at α = 10° and nearly 8 times that at α = 0°. This increase is largely attributed to lateral forces, with the lateral force at α = 20° being three times that at α = 10°.Moreover, the increment in drag from α = 10° to 20° exceeds that from 0° to 10° along the X-axis direction. The resistance of a ship varies significantly at different drift angles. Larger drift angles result in higher lateral forces, which increase the total resistance. For example, as the drift angle increases, the relative angle between the hull and the water flow changes, causing more complex transverse flow and waves, thereby increasing drag. The increase in lateral forces significantly raises the total resistance, and this effect is more pronounced at higher drift angles. Overall, the increase in resistance is closely related to the complexity of transverse flow and changes in the flow field. The analysis of resistance reveals a highly nonlinear growth with increasing drift angle. The total resistance as a function of drift angle (α, in degrees) is best described by a quadratic relationship:

$$R(\alpha) = 10.94 + 0.018\alpha + 0.1775\alpha^2 \tag{10}$$

This fitted relation perfectly matches the calculated data, highlighting an accelerating trend: resistance increased by approximately 164 % from 0° to 10°, and by a further 185 % from 10° to 20°.

The dominance of the α^2 term in the fitted function aligns with the established empirical and theoretical understanding in ship manoeuvring hydrodynamics. At substantial drift angles, the hydrodynamic resistance is primarily governed by the pressure drag due to cross-flow separation. The cross-flow velocity component scales with α, and the resulting drag force, following a quadratic drag law, scales approximately with α^2. The intensifying flow separation, complex vortex dynamics (Section 5.1.6), and modified wave-making (Section 5.1.1) observed in our study are the direct physical manifestations of this accelerating resistance increase.

Table 3 Resistance performance at different drift angles

Drift angle	F_X (N)	F_Y (N)	Total resistance (N)	C_X	C_Y	C_T
0°	10.94	-0.27	10.94	0.0038	-0.0001	0.0038
10°	16.75	23.52	28.87	0.0059	0.0082	0.0101
20°	41.90	70.83	82.30	0.0147	0.0248	0.0288

5.1.3 Velocity

In this section, the velocity field distributions by examining six cross-sections near the bow were analysed. The coordinate axis configuration is the origin is where the bow column meets the waterline; the *X*-axis extends sternward; the *Y*-axis points starboard; and the Z-axis rises from the hull's top. The cross-sectional positions are denoted as *X/Lpp* = 0, 0.025, 0.05, 0.075, 0.125, and 0.15. Figure 8 shows the dimensionless coordinate system division. The green area represents water. The study focuses on the dimensionless axial velocity U_x/U_0, spanwise velocity U_y/U_0, and vertical velocity U_z/U_0 of the fluid in the bow region. Here, U_0 denotes the flow velocity of the relative model in the numerical simulation.

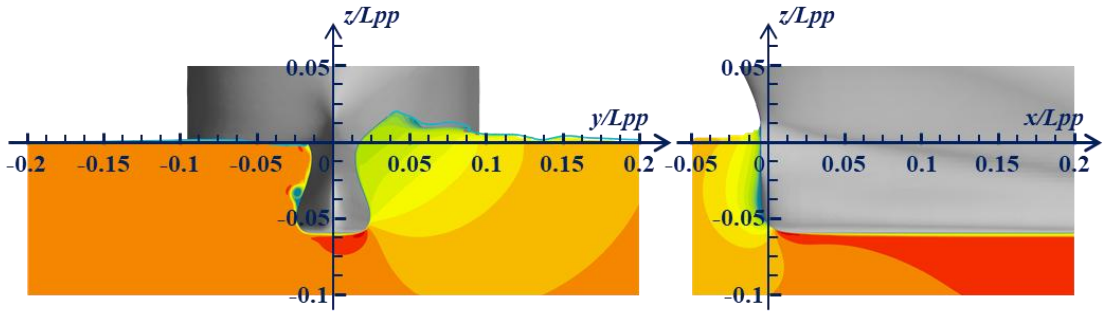

Fig. 8 Dimensionless coordinate system division.

The U_x component characterizes the development trend of the flow field along the ship length direction. Figure 9 shows the dimensionless axial velocity U_x/U_0 of SYSU Hull at the drift angle of 0°. The velocity decreases rapidly upon colliding with the bow, forming a low-velocity zone that expands near the free surface. From Figures 9(a) to 9(d), the velocity gradually increases, creating a high-speed zone at the bottom of the ship, while the velocity boundary layer near the hull initially increases and then decreases. In Figure 9(f), except for the free surface and the bottom of the ship, the velocity field in most areas returns to the incoming flow velocity, indicating relative stability in the *X*-axis direction.

Figure 10 shows the dimensionless axial velocity U_x/U_0 of SYSU Hull at the drift angle of 10°. The velocity boundary layer exhibits an asymmetric distribution. On the starboard side, a small reverse velocity zone forms near the bow, generating an outflow eddy current towards the stern. The velocity field on the port side is lower, accompanied by the phenomenon of water surface rolling. In Figure 10(a), due to the fluid impact on the port side, the velocity component in the *X*-axis direction is smaller than the drift angle of 0 degree, with noticeable water surface rolling at the front of the bow. From Figures 10(b) to 10(f), the velocity gradient near the hull continuously decreases.

Figure 11 shows the dimensionless axial velocity U_x/U_0 of SYSU Hull at the drift angle of 20°. As the drift angle increases to 20°, larger low-speed zones form on both sides of the ship, with pronounced water accumulation. Simultaneously, the high-speed area on the starboard side expands rapidly, showing a trend of being smaller on the left and larger on the right, with an evident flow separation phenomenon at the bow. This flow separation is more apparent from Figures 11(a) to 11(c), and there is a significant pressure difference on both sides of the hull.

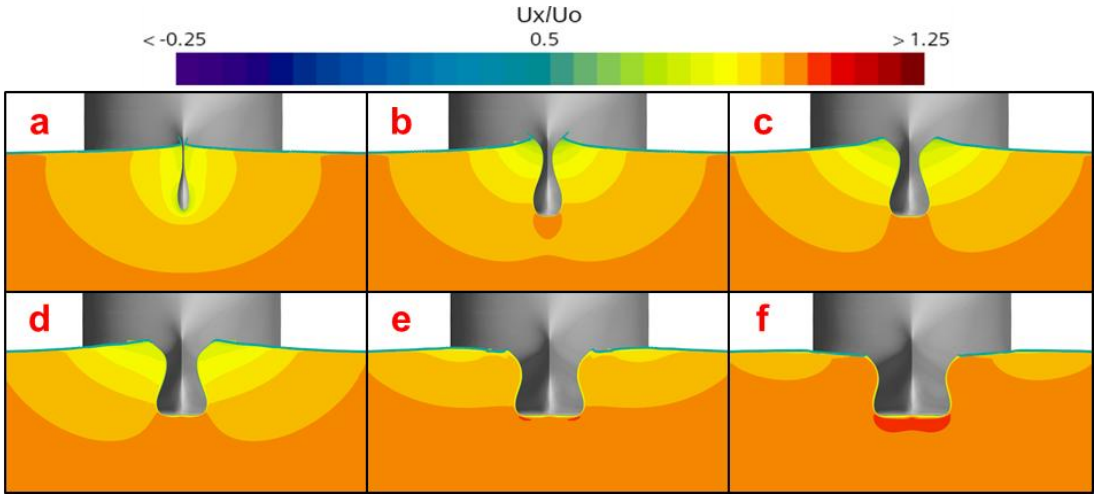

Fig. 9 The dimensionless axial velocity U_y/U_0 of SYSU Hull under straight-ahead: (a) through (f) show cross-sectional views at *X/Lpp* = 0, 0.025, 0.05, 0.075, 0.125, and 0.15, respectively.

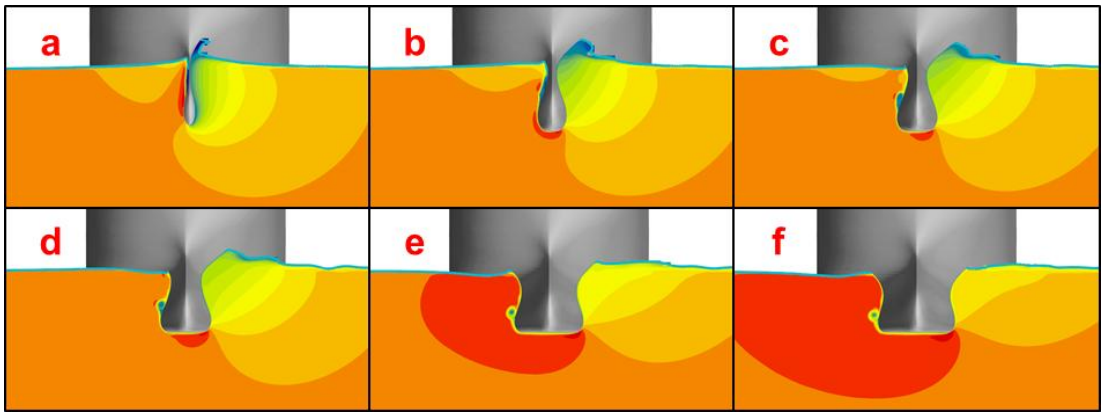

Fig. 10 The dimensionless axial velocity U_x/U_0 of SYSU Hull under static drift of 10-degree conditions: (a) through (f) show cross-sectional views at X/Lpp = 0, 0.025, 0.05, 0.075, 0.125, and 0.15, respectively.

Generally, increasing the drift angle disrupts the water flow path and distribution pattern, exacerbating the asymmetry of the velocity field at the bow, enlarging low-speed zones, and accentuating changes in high-speed regions, particularly emphasizing flow separation and pressure differences. Similar flow separation enhancement with drift angle was noted in the RANS study of Liu et al. [9].

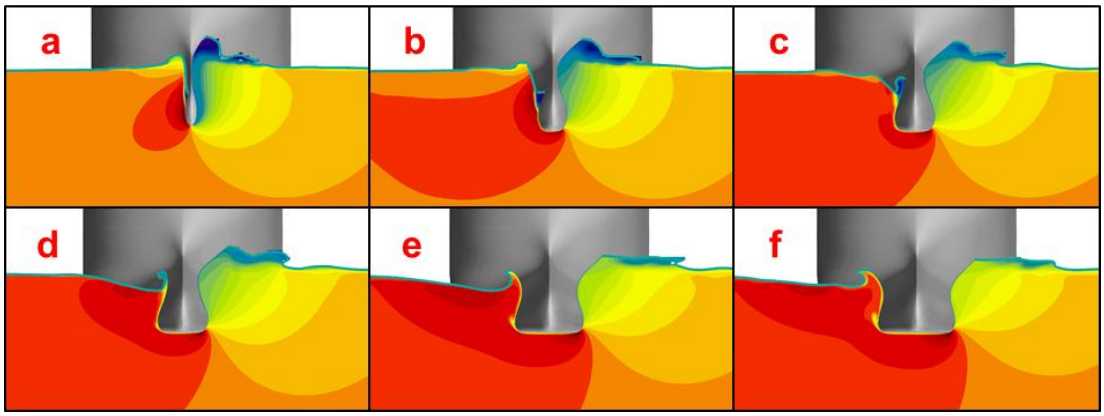

Fig. 11 The dimensionless axial velocity U_x/U_0 of SYSU Hull under static drift of 20-degree conditions: (a) through (f) show cross-sectional views at X/Lpp = 0, 0.025, 0.05, 0.075, 0.125, and 0.15, respectively.

The U_y component characterizes the development trend of the flow field along the beam. Figure 12 is the dimensionless axial velocity U_y/U_0 of SYSU Hull at the drift angle of 0 degree. After the hull collides with the incoming flow, the fluid tends to leave the hull surface, and the velocity gradually decreases from the hull outward, as seen in Figure 12(a). From Figures 12(b) to 12(f), the fluid on both sides of the hull continues to move away, with minimal changes in velocity and velocity gradient. A pair of regions with opposing velocity components form in the lower half-zone, with fluid near the bottom converging directly beneath the hull. The maximum velocity field is located at the point of maximum curvature of the bottom.

Figure 13 is the dimensionless axial velocity U_y/U_0 of SYSU Hull at the drift angle of 10°. Transverse flow causes the flow field below the bow to shift in the positive Y-axis direction, as shown in Figures 13(a) and 13(b). From Figures 13(c) to 13(f), the development of the bow vortex is evident, rotating clockwise. In Figures 13(e) and 13(f), there is a large low-speed area on the starboard side, indicating that the flow field in this region is relatively stable under the hull's occlusion, with minimal lateral movement. Compared to that at the drift angle of 0°, the U_y component and the influence area of the flow field on the port side are larger, and there is no opposing velocity flow field at the bottom of the ship.

Figure 14 is the dimensionless axial velocity U_y/U_0 of SYSU Hull at the drift angle of 20°. Apart from the bottom area's trend towards the positive Y-axis direction, the U_y component on both sides of the bow is negative, indicating that the fluid flows outwards from the sides, moves to the starboard side after passing under the ship, and then flows along the hull. Flow separation occurs near the bow on the port side; the

starboard velocity component first increases in the opposite direction and then decreases, causing fluid to concentrate in the bow depression, which promotes the alignment of the streamlines with the hull surface.

The U_z component characterizes the development trend of the flow field along the depth. Figures 15 to 17 illustrate the U_z of the bow area under different navigation conditions. At the drift angle of 0° (Figure 15), the flow ahead of the bow splits into two parts: upward and downward, as seen from Figures 15(a) to 15(c). The velocity field of the upward part gradually decreases to nearly zero as it approaches the free surface. Conversely, the downward part forms on both sides of the bow, exhibiting a significant negative velocity component. Notably, the vertical downward velocity component is largest on both sides of the bow, while the vertical velocity at the bottom of the ship is close to zero.

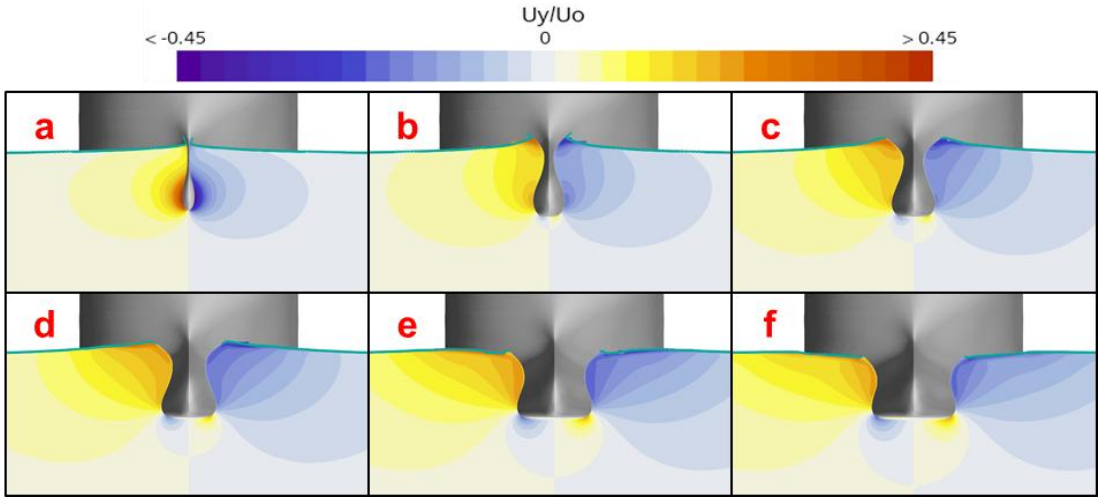

Fig. 12 The dimensionless axial velocity U_y/U_0 of SYSU Hull under straight-ahead: (a) through (f) show cross-sectional views at X/Lpp = 0, 0.025, 0.05, 0.075, 0.125, and 0.15, respectively.

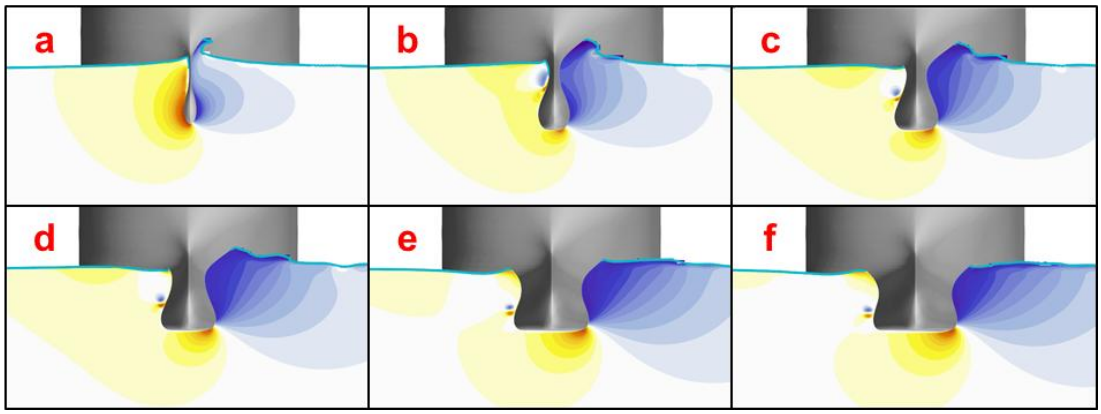

Fig. 13 The dimensionless axial velocity U_y/U_0 of SYSU Hull under static drift of 10° conditions: (a) through (f) show cross-sectional views at X/Lpp = 0, 0.025, 0.05, 0.075, 0.125, and 0.15, respectively.

At a drift angle of 10° (Figure 16), the rollover phenomenon of the free surface is observed on the port side. Simultaneously, the transverse flow on the starboard side leads to the formation of a vertical downward velocity component in this area, indicating the clockwise rotation of the bow vortex. Figures 16(a) to 16(d) depict the emergence and subsequent fallback of this vortex to the free surface. Additionally, the transverse flow rapidly descends along the starboard hull, driving the formation of the downward velocity component in the region and further confirming the clockwise rotation of the bow vortex. This oblique motion also causes a substantial amount of water to rush to the port side, resulting in a wide range of downward velocity on the port side.

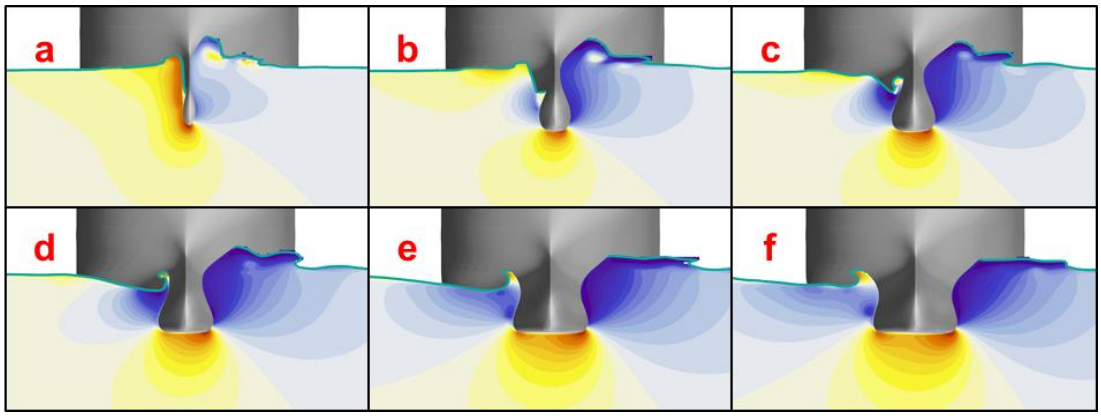

Fig. 14 The dimensionless axial velocity U_y/U_0 of SYSU Hull under static drift of 20-degree conditions: (a) through (f) show cross-sectional views at X/Lpp = 0, 0.025, 0.05, 0.075, 0.125, and 0.15, respectively.

At a drift angle of 20° (Figure 17), the vertical downward velocity distribution on the port side becomes broader, with a larger core high-speed area, leading to faster streamline flow toward the bottom of the ship. From Figures 17(b) to 17(f), the vertical velocity distribution on the starboard side transitions from downward to upward. Combined with the velocity component along the Y-axis, this causes fluid to continue pouring into the hull, resulting in a jump in the free surface and the appearance of a peak. A widespread and persistent region of vertical downward flow is established on the port side of the bow under this condition. This evolution of the velocity field under static drift is fundamentally driven by the corresponding pressure redistribution around the hull, which results in a pronounced asymmetric pressure distribution, as detailed in Section 5.1.5, provides the forcing mechanism: the high pressure on the windward side and low pressure on the leeward side create a strong transverse pressure gradient ($\partial p / \partial y$). This gradient directly drives the positive U_y component (flow from windward to leeward) observed in the lower hull and bottom regions (Figures 13 and 14), constituting the cross-flow. This cross-flow, when combined with the hull's geometry, is deflected downward on the leeward side, resulting in the sustained vertical downwash (negative U_z, Figure 17). Concurrently, the large area of low U_x on the leeward bow (Figures 10 and 11) corresponds to the flow separation zone, which is initiated and sustained by the adverse pressure gradient in that region. Therefore, the velocity field is not merely an outcome but a dynamic response that visually maps the integrated effect of the hull's asymmetric pressure distribution under drift.

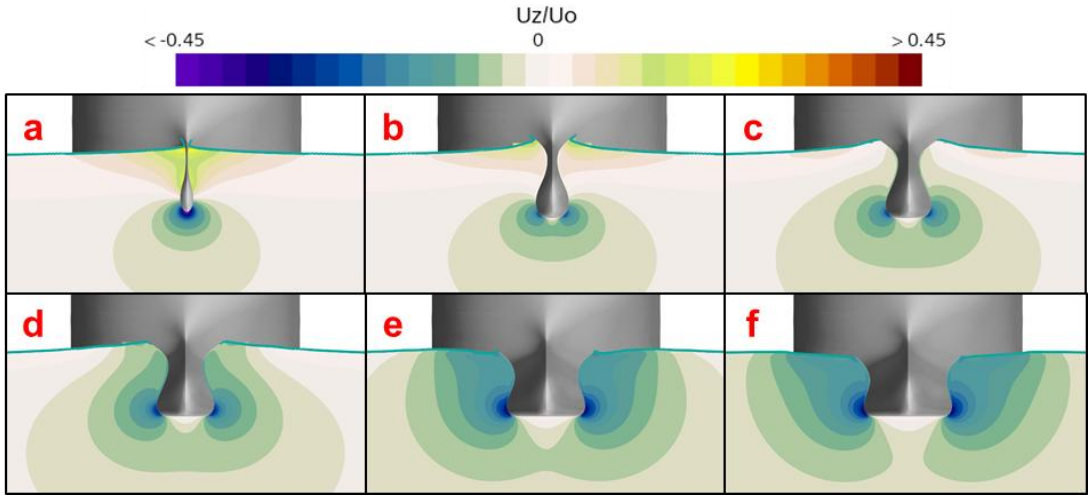

Fig. 15 The dimensionless axial velocity U_z/U_0 of SYSU Hull under straight-ahead: (a) through (f) show cross-sectional views at X/Lpp = 0, 0.025, 0.05, 0.075, 0.125, and 0.15, respectively.

Studies indicate that such downward flow induced by wave breaking serves as a key mechanism driving the downward transport of bubbles [4]. Therefore, the strong and sustained downward flow observed in the present simulation suggests that air entrainment and downward transport are more likely to occur in

the bow region at this drift angle, thereby significantly increasing the potential risk of bubble interference with the side-mounted multi-beam acoustic equipment.

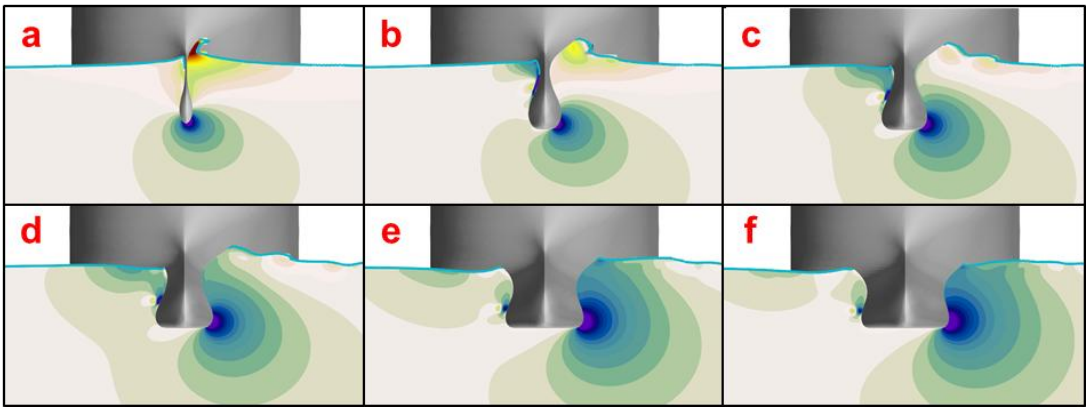

Fig. 16 The dimensionless axial velocity U_x/U_0 of SYSU Hull under static drift of 10° conditions: (a) through (f) show cross-sectional views at X/Lpp = 0, 0.025, 0.05, 0.075, 0.125, and 0.15, respectively.

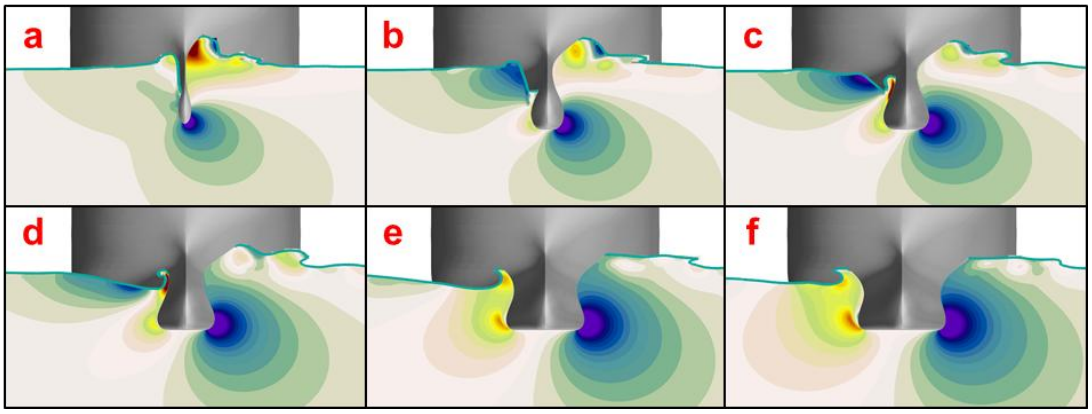

Fig. 17 The dimensionless axial velocity U_x/U_0 of SYSU Hull under static drift of 20° conditions: (a) through (f) show cross-sectional views at X/Lpp = 0, 0.025, 0.05, 0.075, 0.125, and 0.15, respectively.

5.1.4 Streamline

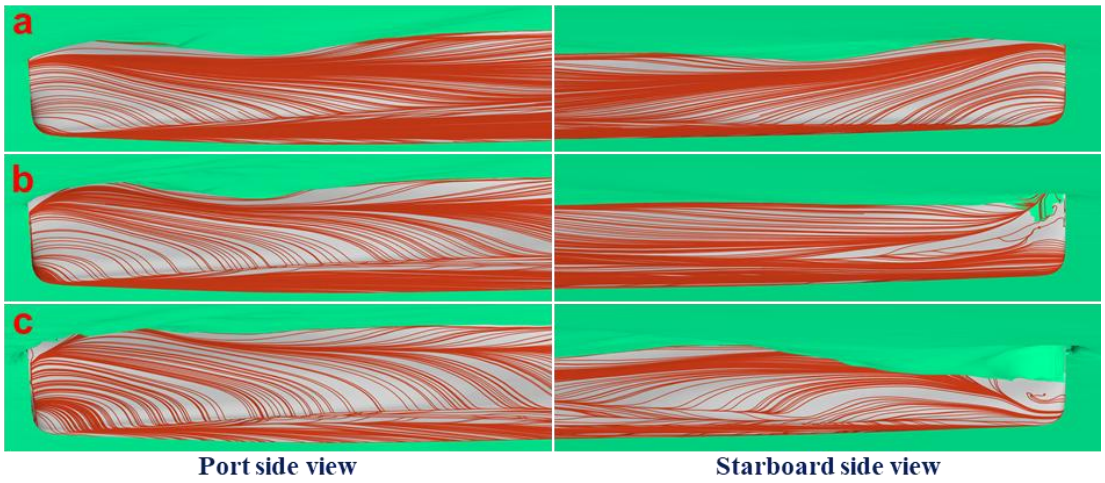

Fig. 18 The streamlines around SYSU hull: under (a) straight-ahead; (b) static drift of 10° and static drift of 20° conditions.

Figure 18 is the streamlines around SYSU hull at various drift angles. At the drift angle of 0° (Figure 18(a)), the streamlines are roughly parallel to the hull and relatively uniform. The direction of fluid

flow around the bow changes little, with streamlines flowing smoothly over the hull, experiencing minimal flow separation. The curvature of the streamlines around the hull is minimal, leading to a relatively symmetric distribution. At the drift angle of 10° (Figure 18(b)), the streamlines begin to show noticeable curvature, particularly around the bow. Streamlines on one side curve more distinctly, and the spacing between them becomes uneven, increasing the asymmetry in the flow around the hull, while the other side remains relatively straight. Flow separation starts to significantly affect the streamline shape, making the flow pattern more complex. At the drift angle of 20° (Figure 18(c)), streamlines exhibit pronounced curvature and asymmetry. High angles of attack lead to a more asymmetric distribution of streamlines on either side of the hull, with the flow separation region significantly expanding. The asymmetry in the flow intensifies, making the entire flow field more twisted and irregular.

Overall, as the drift angle increases, the streamlines along the length of the hull transition from uniform and parallel to curved and asymmetric. This change reflects the complex effects of flow separation, pressure differences, and fluid dynamics, resulting in increasingly intricate streamline behaviour around the hull. The acoustic equipment on one side of the research ship tends to have better operating conditions during oblique navigation, though the equipment on the opposite side might experience increased interference.

5.1.5 Pressure

Figure 19 illustrates the surface pressure distribution on the ship model at various drift angles. Generally, a positive pressure area forms on the upstream surface of the hull, while negative pressure areas develop on the bottom and backflow surfaces. As the drift angle increases, the overall hydrodynamic pressure on the vessel changes significantly. A distinct low-pressure zone develops in the mid-ship area near the bottom of the hull. The port side experiences a greater degree of negative pressure compared to the starboard side, with a more pronounced pressure gradient observed. In the bow area, the transition from a positive to a negative pressure zone causes fluid to be directed towards the underside of the hull. On the port side, hydrodynamic pressure on the hull's surface decreases progressively along the *Z*-axis, with steeper pressure gradients at higher drift angles. As the drift angle reaches 20°, the high-negative-pressure area in the bilge expands towards the midsection of the hull, increasing the absolute pressure and promoting fluid movement towards the bottom. This condition may lead to bubble formation and could interfere with multi-beam sonar equipment. The underlying process is closely linked to bubble transport under pressure gradients and local turbulence modulation. The complex pressure and vortex fields at the bow are likely to modulate the local turbulence, thereby influencing the initial size distribution and the consequent acoustic scattering characteristics of the entrained bubbles [32], which directly relates to their potential for equipment interference. On the starboard side, a significant negative pressure zone develops at the bow, causing fluid to adhere closely to the hull and resisting movement towards the bottom. At a 10° drift angle, a notable low-pressure zone is present in the central region of the ship. By 20°, a vertical negative pressure channel emerges, enabling stable backward fluid flow.

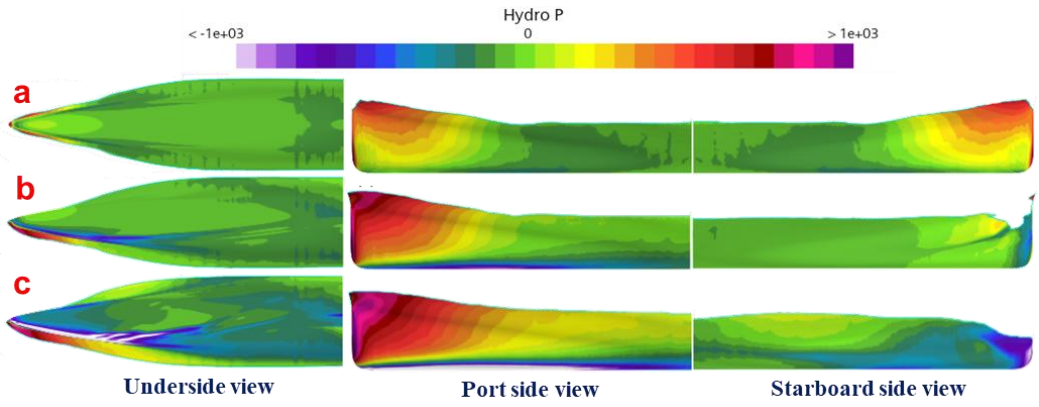

Fig. 19 The distribution of hydrodynamic pressure on the hull surface: under (a) straight-ahead; (b) static drift of 10° and static drift of 20° conditions.

Overall, as the drift angle increases, the hydrodynamic pressure distribution on the hull surface transitions from uniform to significantly asymmetric and complex, primarily due to changes in fluid flow and flow separation phenomena. This trend of increasing pressure asymmetry with drift angle is consistent with RANS-based findings reported by Liu et al. [9].

5.1.6 Vortex structure distribution

In this study, the Q criterion (Iso-surfaces of $Q = 120/s^2$) were utilized to thoroughly describe and analyse the vortex structures present in the flow field. By examining different drift angles, the distribution of various vortex types at the bottom of the ship were observed. The vortex system in the flow field can be roughly divided into four parts: fore-body keel vortices (FBKV), deadwood vortices (DV), stern vortices (SV), and free surface vortices (FSV). Figures 20, 21, and 22 are the vortex system around the hull at the drift angle of 0°, 10° and 20°, respectively. At the drift angle of 0° (Figure 20), vortices are symmetrically distributed along the central axis of the hull. As the drift angle increases, the vortex tubes shift towards the starboard side, and the strength and influence range of the vortices increase. At the drift angle of 10° (Figure 21), significant movement of the free surface vortex (FSV) from the port side of the bow towards the starboard side were observed. Additionally, smaller fore-body side vortices (FBSV) were generated near the bow. Compared to that at the drift angle of 0°, fore-body keel vortices (FBKV) exhibit a more pronounced displacement and increased intensity. As the vortices move toward the midship, a gradual division occurs into three smaller vortex tubes, with those closer to the ship weakening and dissipating over time. FBKV extends aft through the hull, further complicating the stern vortex (SV). Furthermore, increasing drift angles enhance deadwood vortices (DV), which can disrupt the development of Kelvin waves. Oblique bilge vortices (OBV) are also observable but relatively minor, influenced by the model's low speed and shallow drift angle. At the drift angle of 20° (Figure 22), the extrusion of the free surface vortex (FSV) becomes more pronounced, leading to greater accumulation on the port side of the bow and more intense release on the starboard side. The fore-body side vortices (FBSV) grow larger and become more complex. The fore-body keel vortices (FBKV) pass from the port side to the starboard side of the hull earlier, resulting in the formation and eventual dissipation of two larger vortex tubes on the port side. The intensity of the deadwood vortices (DV) increases significantly, extending further towards the stern. Additionally, the strength of the stern vortex (SV) is markedly enhanced, forming a larger vortex tube that propagates farther. The transform vortices also become more intricate, with numerous small vortices forming at the stern, which interfere with the Kelvin wave. Compared to that at the drift angle of 10°, oblique bilge vortices (OBV) are now clearly present and can interfere with the sonar area. To mitigate the impact of these eddy currents on sonar performance, the installation of diversion covers, a Gondola, or other equipment at this location may be considered.

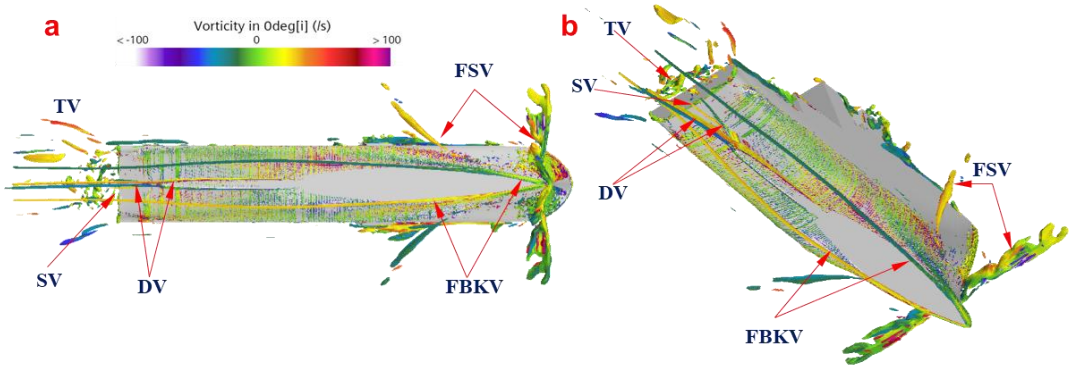

Fig. 20 Vortex system around the hull under straight-ahead conditions: (a) overall view; (b) bottom view

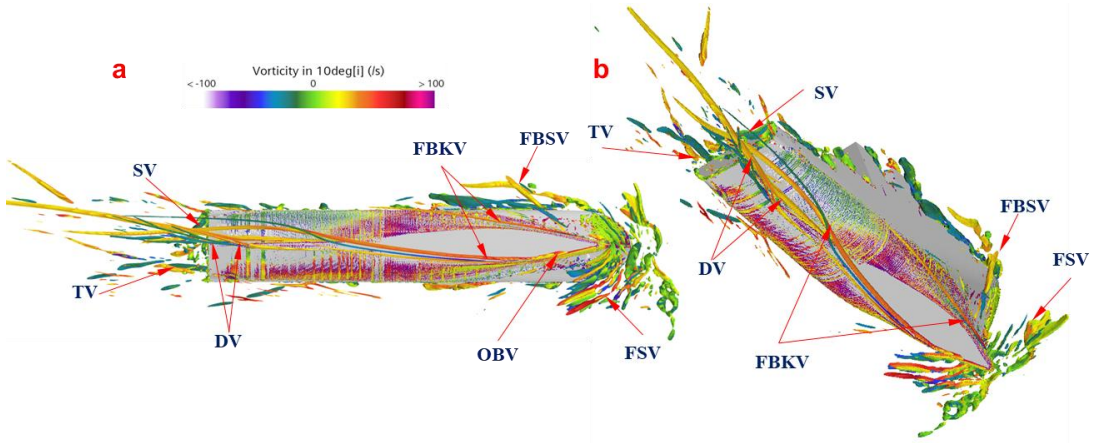

Fig. 21 Vortex system around the hull under static drift of 10° conditions: (a) overall view; (b) bottom view.

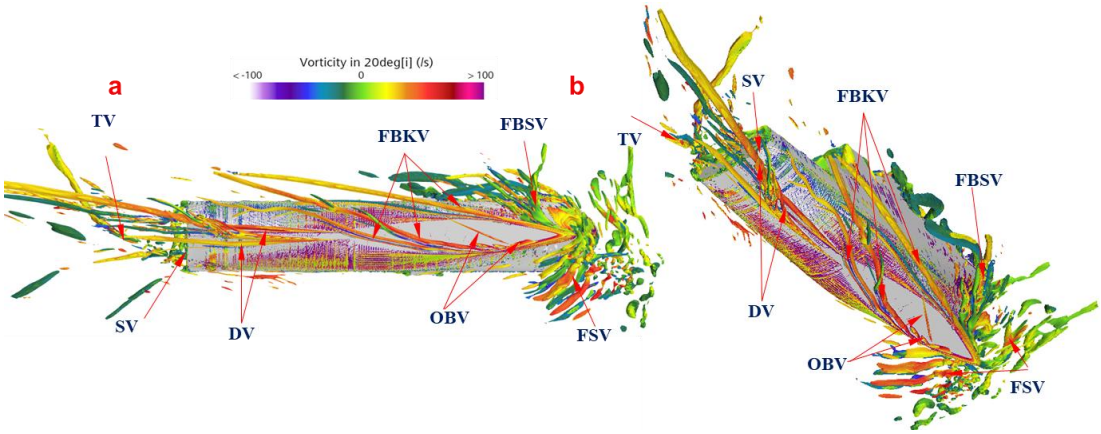

Fig. 22 Vortex system around the hull under static drift of 20° conditions: (a) overall view; (b) bottom view.

5.1.7 Vorticity distribution of slices

Six cross-sections near the bow were selected to analyse the vorticity intensity and distribution for the vorticity component along the X-axis. Figure 23 is the axial vorticity Omega x of SYSU Hull at the drift angle of 0°.

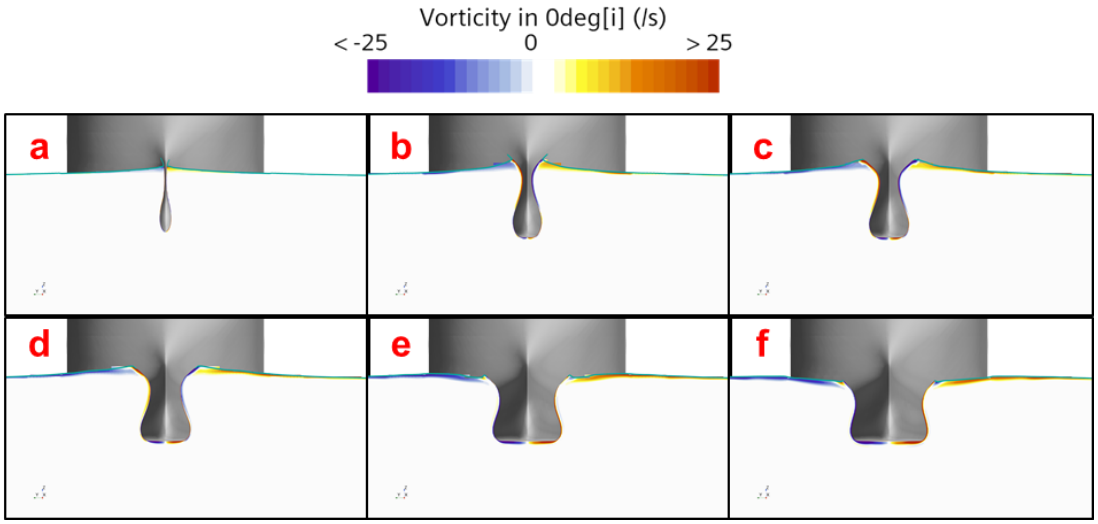

Fig. 23 The axial vorticity Omega *x* of SYSU Hull under straight-ahead: (a) to (f) show cross-sectional views at *X/Lpp* = 0, 0.025, 0.05, 0.075, 0.125, and 0.15, respectively.

Figures 23(a) to 23(f) show the cross-sectional views at *X/Lpp* = 0, 0.025, 0.05, 0.075, 0.125, and 0.15, respectively. The vorticity is primarily concentrated on the hull surface and near the free surface at the drift angle of 0°. This consists mainly of surface vortices generated by hull-water collisions and small rolling vortices near the free surface.

Figure 24 is the axial vorticity Omega x of SYSU Hull at the drift angle of 10°. Figures 24(a) to 24(f) show the cross-sectional views at *X/Lpp* = 0, 0.025, 0.05, 0.075, 0.125, and 0.15, respectively. At the angle of α = 10°, positive vorticity gradually develops on the port side. Here, the flow impact creates a free surface roll towards the port side, while positive vorticity persists at the bottom of the ship. Conversely, the starboard side exhibits predominantly negative vorticity, clearly demonstrating the formation and evolution of bow vortices.

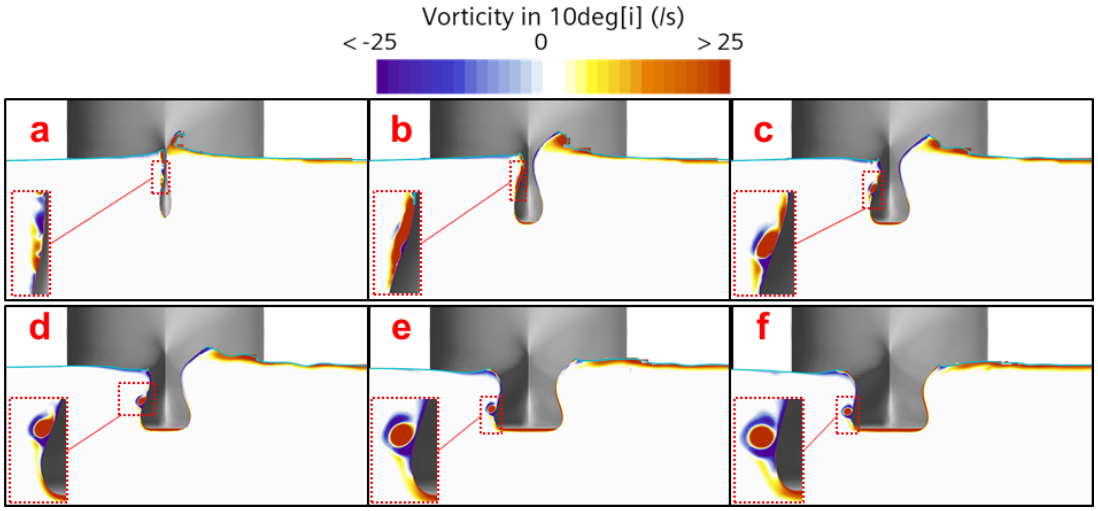

Fig. 24 The axial vorticity Omega *x* of SYSU Hull under static drift of 10° conditions: (a) to (f) show cross-sectional views at *X/Lpp* = 0, 0.025, 0.05, 0.075, 0.125, and 0.15, respectively.

Figure 25 is the axial vorticity Omega x of SYSU Hull at the drift angle of 20°. Figures 25(a) to 25(f) show the cross-sectional views at *X/Lpp* = 0, 0.025, 0.05, 0.075, 0.125, and 0.15, respectively. At a drift angle of 20°, the port side experiences more vigorous free surface disturbances from upstream flow compared to 10°, resulting in a broader area of positive vorticity near the free surface extending towards the bow's aft end. Meanwhile, the starboard side shows a smaller area of negative vorticity affected by cross flows, leading to fluid rising along the hull surface and moving rearward within the flow field. Figures 25(c) to 25(f) depict the bow vortex development process, revealing larger vortex diameters compared to the 10°. These vortices exhibit a circular structure with reverse rotation, devoid of external negative vorticity.

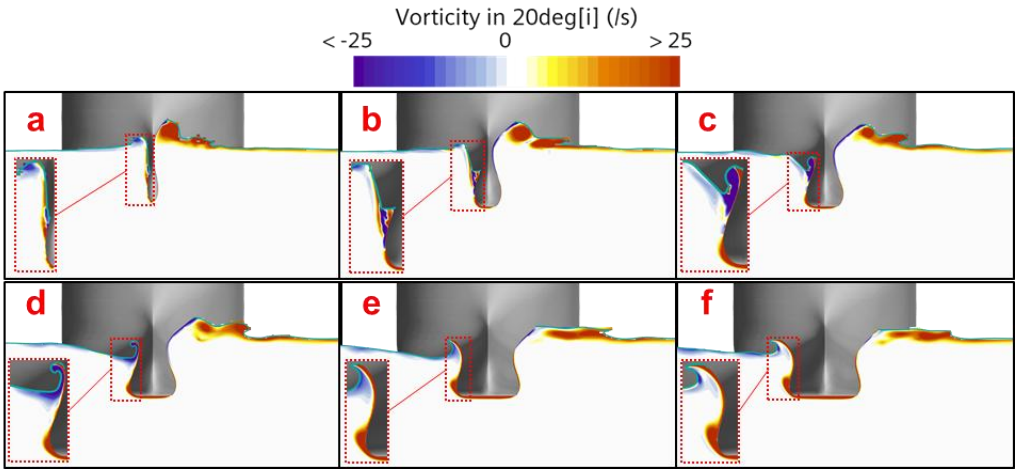

Fig. 25 The axial vorticity Omega *x* of SYSU Hull under static drift of 20° conditions: (a) to (f) show cross-sectional views at *X/Lpp* = 0, 0.025, 0.05, 0.075, 0.125, and 0.15, respectively.

5.2 Manoeuvre yaw status

5.2.1 Free surface

Figure 26 shows the free surface waveform of the Model SYSU under manoeuvring oblique navigation. It shows the perspective of observation from the bottom of the ship to the free surface. The left side is the starboard and the right side is the port.

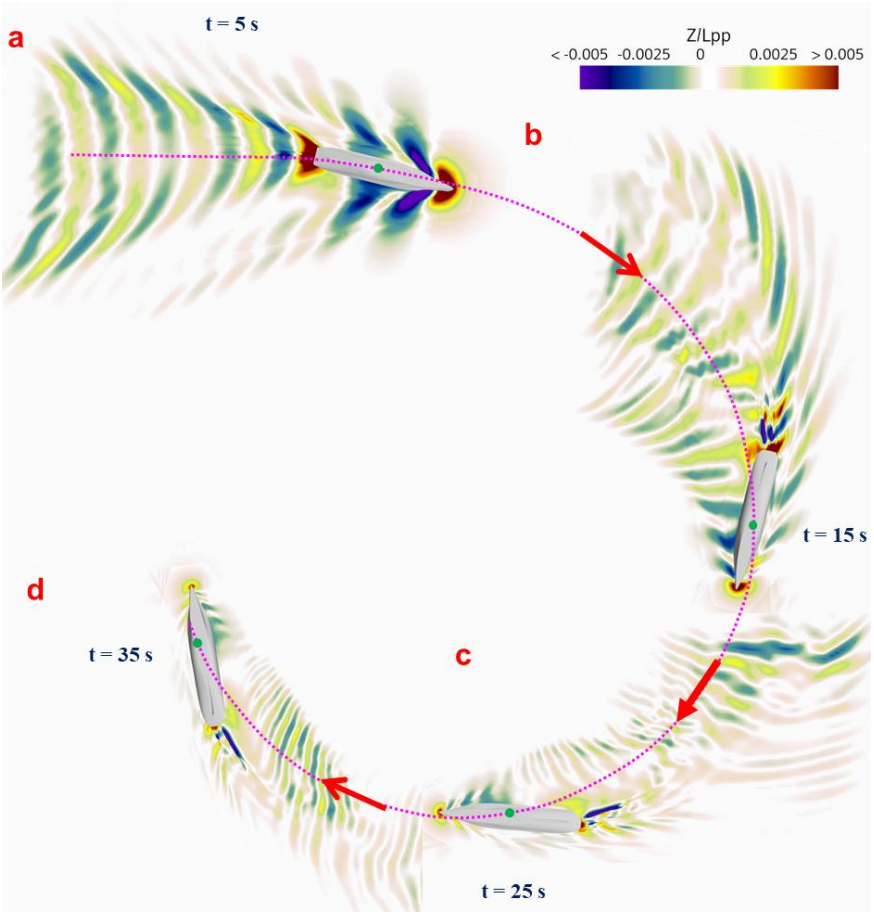

Fig. 26 Free surface elevation contours around SYSU hull during rotation motion: (a) to (d) show instantaneous time at t = 5 s, 15 s, 25 s, and 35 s, respectively.

Figures 26(a) to 26(d) are the waveforms at 5 s, 15 s, 25 s, and 35 s from the beginning of rotation. In Figure 26(a), the Kelvin wave system near the hull is still clearly visible. However, due to the conversion of the starboard to the inflow surface, the wave system is no longer symmetrical and close to the other side. In general, the disturbance of the flow field is not as severe as that at the drift angle of 10°. In Figure 26(b), the waveforms on both sides of the hull are obviously different. The waveform of the port side is more obvious, and the amplitude is larger than that of the starboard. At the same time, the amplitude of the wave near the bow is obviously reduced, and there is a peak area on the starboard side. The waveform of the stern is squeezed. In Figure 26(c), due to the decrease of speed caused by rotation, the overall wave-making of the ship has been significantly reduced, and the wave-making generated by the port side is still obvious, while the wave-making generated by the starboard is limited to the vicinity of the hull. The difference between the waveforms of Figures 26(c) and 26(d) is small, indicating that the ship has entered a state of steady rotation, and the free surface on the left side of the bow is lower than that on the right side, and a trough area appears.

5.2.2 Resistance

Table 4 presents the resistance and total resistance of Model SYSU along the X-axis (length direction) and Y-axis (beam direction) at various rotation times, with each resistance referenced to the ship-fixed

coordinate system. Following the onset of rotation, resistance increases significantly, similar to that at the drift angle of 10°, where X-axis resistance rises, subjecting the ship to approximately 24 N of lateral force. At 15 s, resistance peaks, accompanied by the highest lateral force among the four-time points. During the rotation process, total resistance generally remains lower than during that at the drift angle of 20°. Both total drag and Y-axis resistance initially increase before decreasing. Notably, resistance from 25 to 35 s decreases compared to 15 s, with a smaller drop in drag by 25 s indicating a stabilized rotational navigation state. X-axis drag exhibits a monotonous decrease, approaching stability, as thrust remains constant. Consequently, total drag surpasses thrust, leading to reduced speed, with thrust primarily countering lateral drag.

Table 4 Resistance performance at different swing times

Turning time	F_X (N)	F_Y (N)	Total resistance (N)	C_X	C_Y	C_T
5 s	11.64	-24.04	26.71	0.0041	-0.0084	0.0094
15 s	9.35	-32.72	34.03	0.0033	-0.0115	0.0119
25 s	6.95	-25.27	26.21	0.0024	-0.0089	0.0092
35 s	6.22	-22.97	23.79	0.0022	-0.0080	0.0083

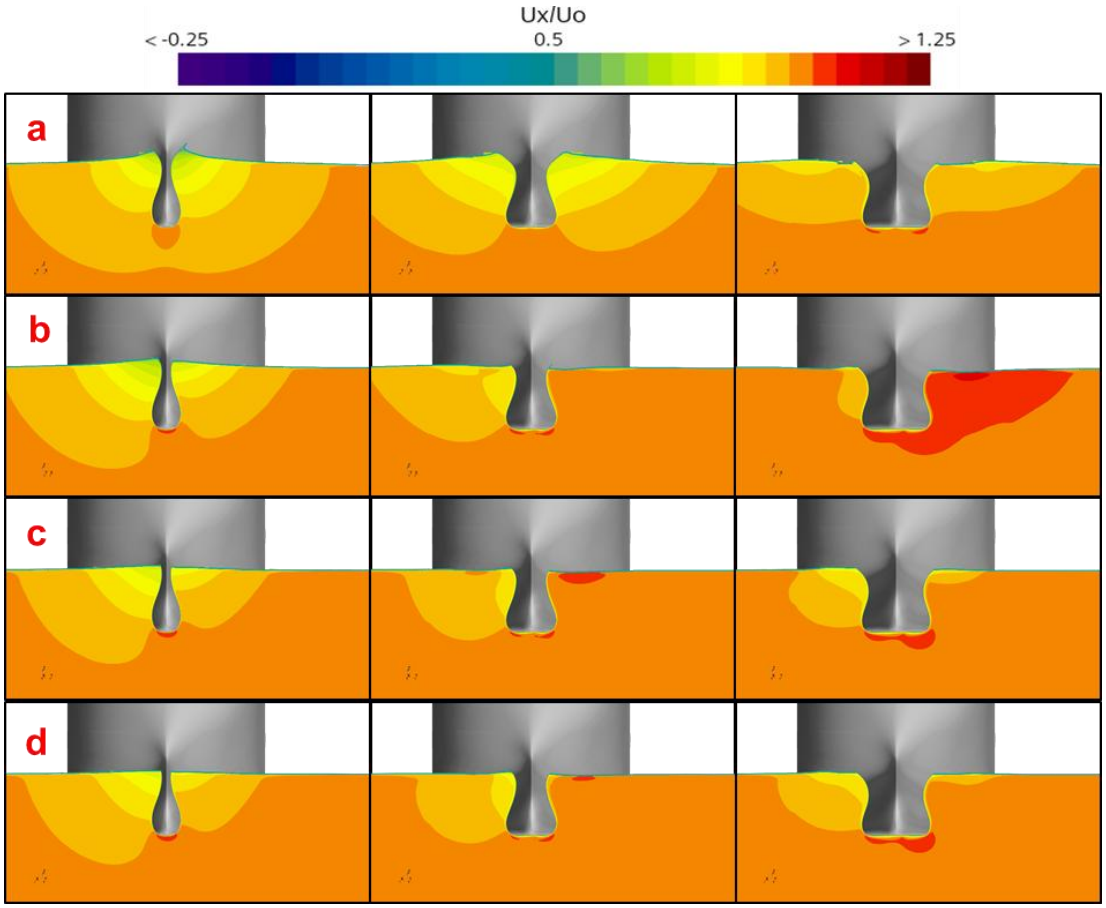

Fig. 27 The dimensionless axial velocity U_x/U_0 of SYSU Hull during rotation: (a) to (d) show instantaneous time at t = 5 s, 15 s, 25 s, and 35 s, respectively.

5.2.3 Velocity

Figure 27 illustrates the U_x/U_0 of the bow area during rotation. At 5 s, the velocity slightly decreases as rotation begins. The velocity distribution along the X-axis remains similar to that at the drift angle of 0° yet asymmetrical areas have emerged on the left and right sides. By 15 s, the velocity field distribution of the ship hull shows noticeable asymmetry between its left and right sides. Despite a small actual drift angle and

reduced velocity, the flow field disturbance is much less intense compared to that at the drift angle of 10°. Unlike at 5 s, oblique motion now induces a high-speed zone near the port side of the leeward flow. By 25 s, the gradient of the velocity boundary layer decreases significantly, indicating a notable velocity reduction. High-speed zones are observed both portside and beneath the ship, though only the latter persists. At 35 s, while the velocity boundary layer and high-speed area continue to diminish, the overall change is not substantial, signifying stabilization into a steady rotation state. The high-speed zone beneath the ship remains relatively unchanged in size, indicating a stable flow field less affected by rotation.

Figure 28 depicts the U_y/U_0 component in the bow region during rotation. At 5 s, the majority of the velocity in the flow field diverges to both sides of the hull, causing fluid to depart from the hull surface. Conversely, the velocity component at the bottom of the ship is opposite, with water gathering beneath the hull, illustrating asymmetry in the flow field on both sides. By 15 s, the starboard side encounters water, and high-speed flow exits the hull area. Unlike at the drift angle of 10°, there remains an area where fluid gathers beneath the ship, indicating that the flow through the geometric inflection point of the ship's side towards its bottom does not fully disperse the water flow on the opposite side. At both 25 s and 35 s, the flow field in each section exhibits minimal variation, indicating a relatively stable state. Compared to 15 s, there is only a slight decrease in velocity absolute value, and this reduction is less than that observed in the X-axis velocity component at the same time, suggesting that the Y-axis flow field is less affected by rotation.

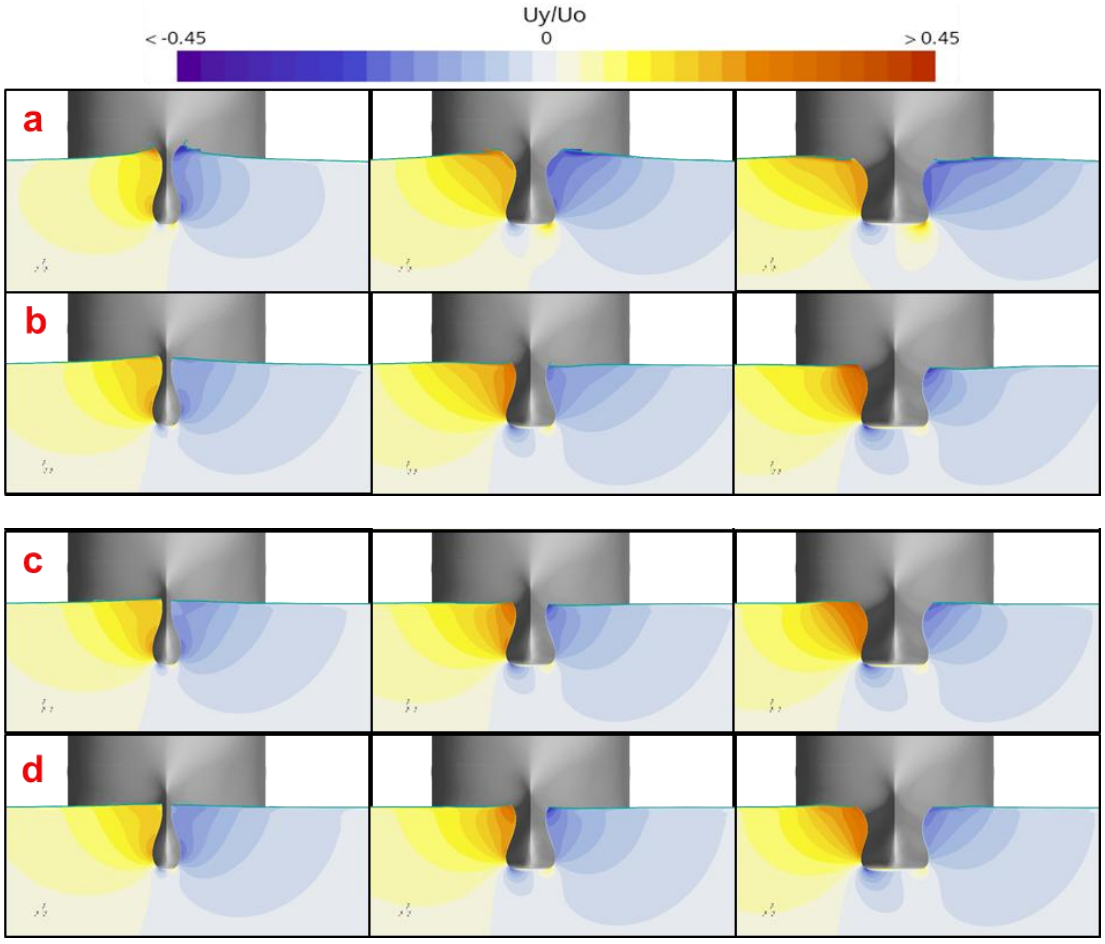

Fig. 28 The dimensionless axial velocity U_y/U_0 of SYSU Hull during rotation: (a) through (d) show instantaneous time at t = 5 s, 15 s, 25 s, and 35s, respectively.

Figure 29 illustrates the U_z/U_0 component in the bow area at 5 s and 15 s during rotation. At 5 s into the turn, the vertical velocity distribution closely resembles that at the drift angle of 0°.

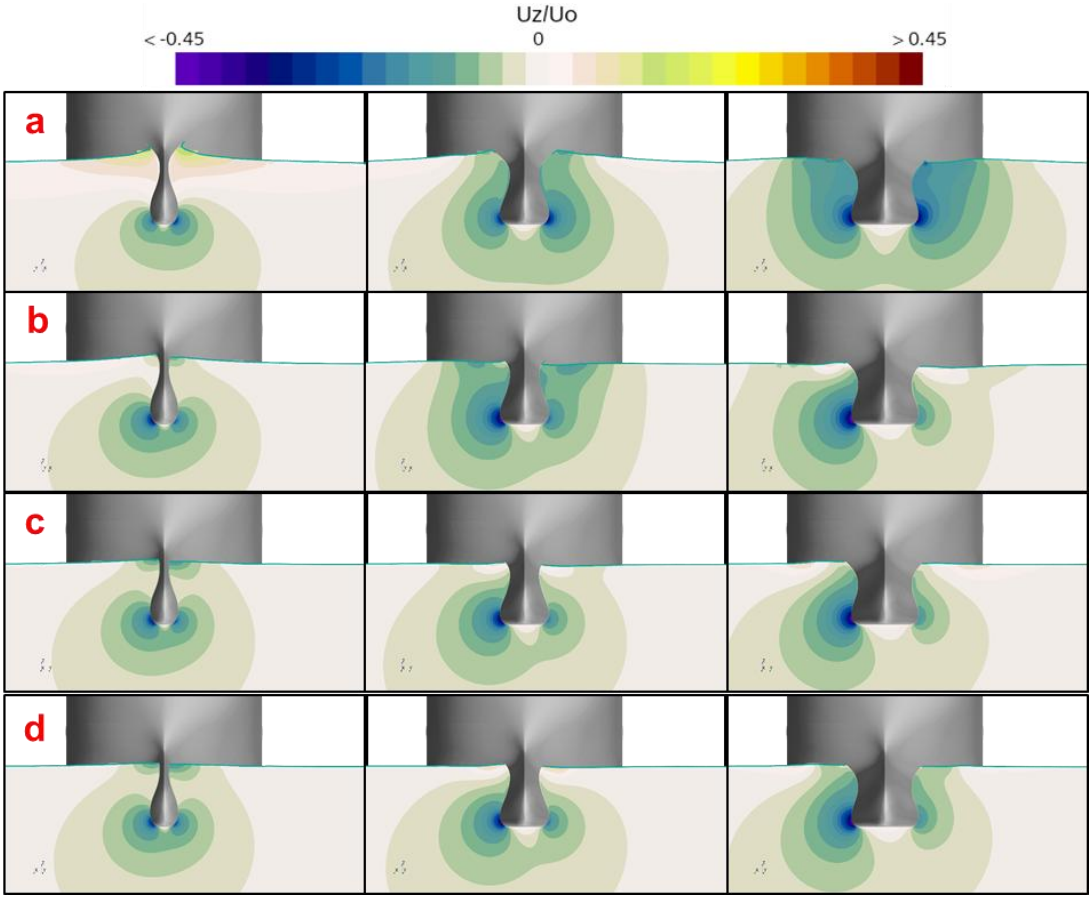

Fig. 29 The dimensionless axial velocity U_z/U_0 of SYSU Hull during rotation: (a) to (d) show instantaneous time at t = 5 s, 15 s, 25 s, and 35 s, respectively.

The port side exhibits slightly higher vertical velocity compared to the starboard side, possibly due to upstream effects. Concurrently, there is a region near the bottom of the ship where vertical velocity approaches zero, indicating water flow converging from both sides towards the middle before accelerating towards the stern. By 15 s of rotation, the oblique flow on the starboard side leads to a broader range of downward velocity distribution, which will quickly cause the bow streamline and bubbles to sweep down. In comparison to that at the drift angle of 10°, the distribution area and extreme values of vertical velocity are smaller during oblique navigation. Little variation is observed in the flow field at 25 s and 35 s, with a slight reduction in extreme values of vertical velocity near the bow's core area. Additionally, there is an opposite trend in the vertical velocity near the free surface between 25 s and 15 s; specifically, the vertical velocity near the free surface increases in some instances and decreases in others. Overall, a consistent vertical downward flow field near the bow persists throughout the rotary motion process, potentially impacting the operation of acoustic equipment.

In the turning case, the dynamically evolving pressure field similarly explains the temporal changes in the velocity components. The pressure distribution provides the essential link between the ship's imposed motion and the complex, three-dimensional velocity structure observed in its wake. This pressure-velocity coupling is the key to understanding the resultant hydrodynamic forces and the evolution of vortical structures.

5.2.4 Streamline

Figure 30 is the streamlines around SYSU hull during rotation. Figures 30(a) to 30(d) show instantaneous time at t = 5 s, 15 s, 25 s, and 35 s, respectively. According to Figure 30, focusing on the port side of the hull, the first vertical drift dd was used as a reference, and four equally spaced streamlines were analysed to observe how streamline distribution varies across different rotation times. At t = 5 s, most

streamlines originate from the bow and pass along the bottom of the ship, similar to that at the drift angle of 0°. However, at subsequent time points, the upper part of the bow's streamlines extends towards the free surface behind the stern. This extension helps reduce surface rollover and minimizes bubble flow towards the bottom of the ship, thereby decreasing interference with multi-beam equipment. The streamline distribution on the starboard side exhibits similar characteristics, warranting further comparative analysis. Auxiliary lines were added based on the starboard's bottom streamline sweeping down to the bottom of the ship at t = 5 s to determine streamline distribution at other time points. For the port side, the bottom streamline at t = 25 s extends the furthest and performs best across all time points. On the starboard side, the streamline distribution is optimal at 25 s, akin to the configuration observed at the drift angle of 0° at 5 s, while it deteriorates notably by 35 s. Hence, the complex flow dynamics during rotary motion and the gradual decrease in speed significantly influence streamline distribution.

Overall, as the ship rotates, the relative angle of the hull continuously changes, causing alterations in the shape and distribution of the streamlines. In the rotational movement, the streamlines at different moments will change according to variations in rotational angle, vortex formation, free surface changes, and local flow characteristics. Different rotational angles induce varying fluid dynamics effects, affecting the curvature and distribution pattern of the streamlines.

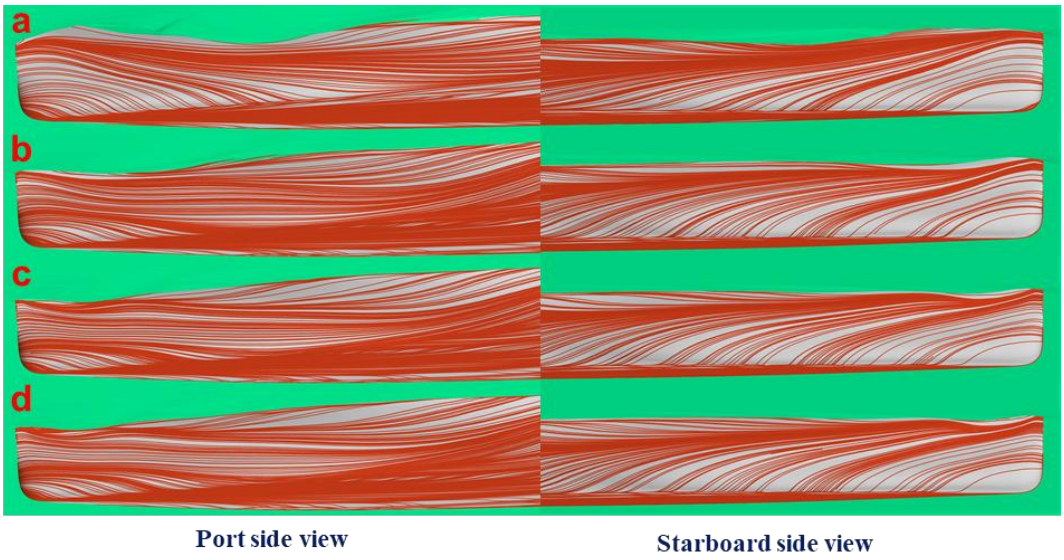

Fig. 30 The streamlines around SYSU hull during rotation: (a) to (d) show instantaneous time at t = 5 s, 15 s, 25 s, and 35 s, respectively.

5.2.5 Pressure

Figure 31 depicts the hydrodynamic pressure distribution along the bottom and sides of Model SYSU at various turning times, with the area above the free surface omitted. At 5 s, the pressure distribution shows minimal disparity between both sides of the hull, with slightly higher extreme pressures noted on the port side. By 15 s, a pronounced low-pressure area emerges in the middle of the bow, indicative of relatively stable flow. However, notable pressure gradients persist on the starboard side, facilitating continued downward streamlining, consistent with prior research findings. As time progresses to 25 s and 35 s, hydrodynamic pressures diminish significantly due to the deceleration of the vessel. This reduction in speed correlates with the observed decrease in pressure gradients and overall pressure levels across both sides of the hull.

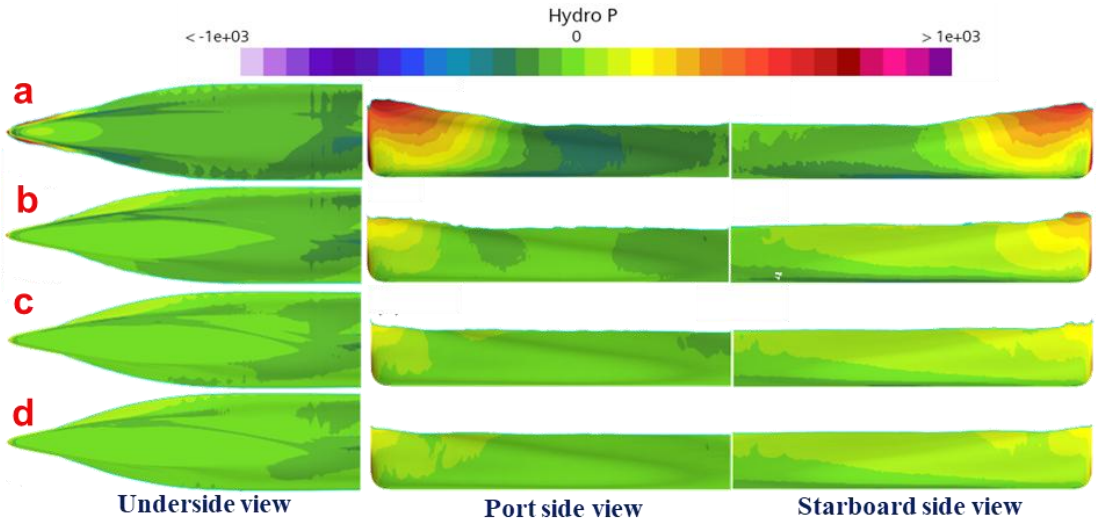

Fig. 31 The distribution of hydrodynamic pressure on the hull surface during rotation: (a) to (d) show instantaneous time at t = 5 s, 15 s, 25 s, and 35 s, respectively.

5.2.6 Vortex structure

Figure 32 illustrates the bottom vortex structure at different turning times. Figure 33 is the closeup view of the vortex structure around bow and stern region under different rotation time. The green background represents the free surface, with the starboard depicted at the top and the port at the bottom, visualized using vorticity iso-surfaces ($Q = 120/\mathrm{s}^2$).

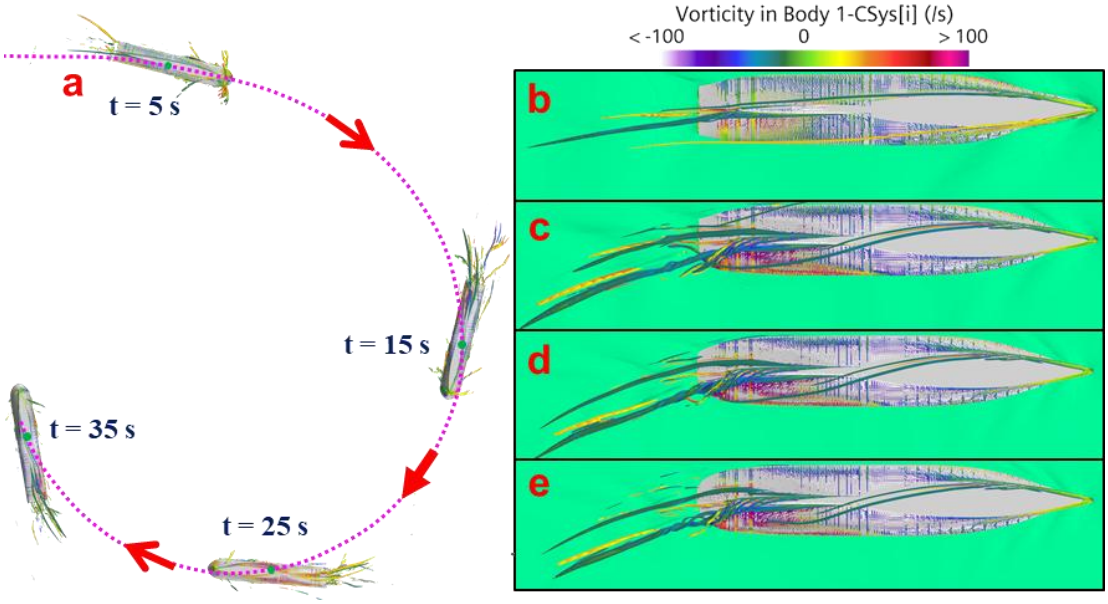

Fig. 32 Vortex structure around the hull during rotation motion: (a) Over all view; (b) to (e) show instantaneous time at t = 5 s, 15 s, 25 s, and 35 s, respectively.

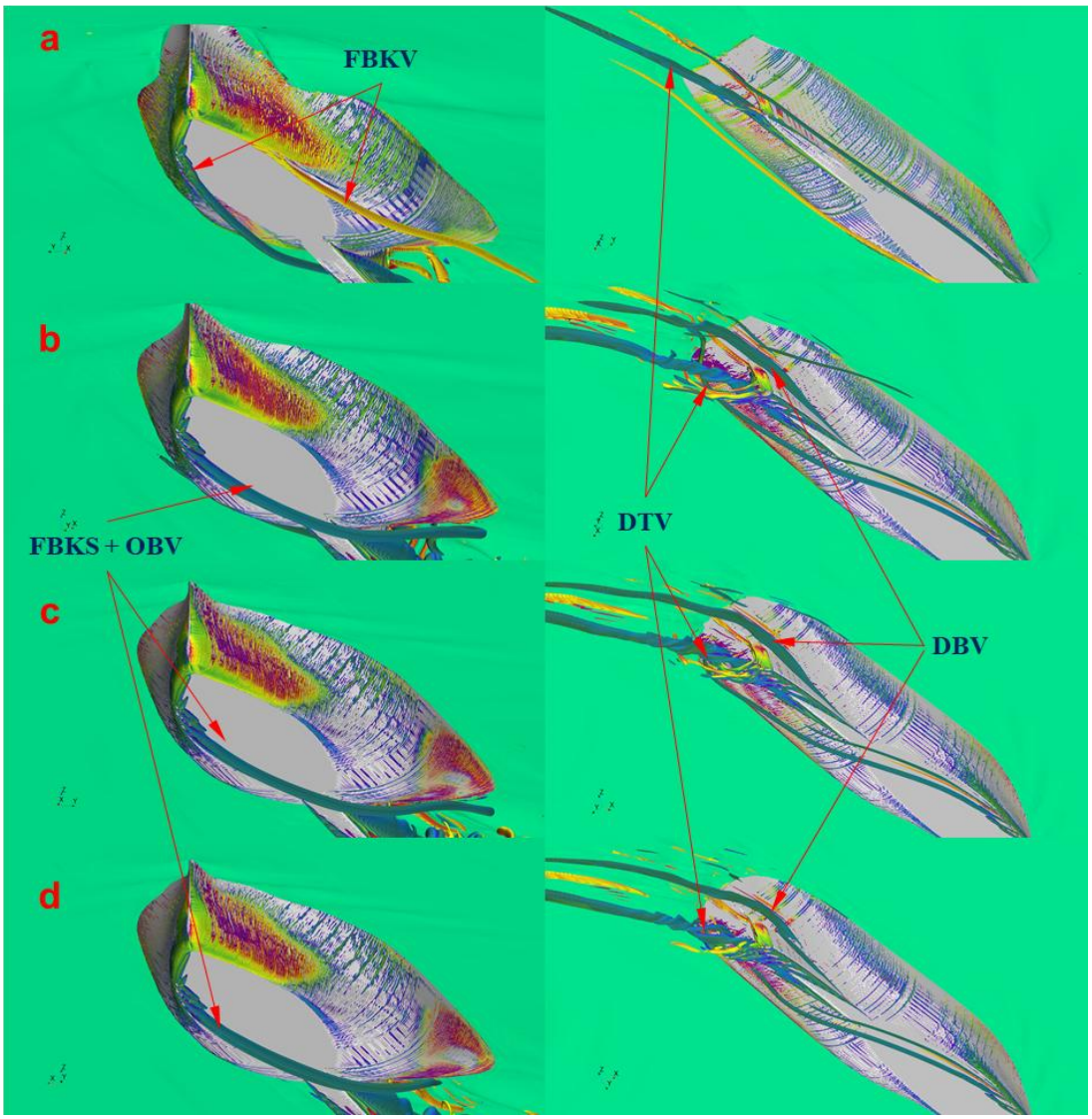

Fig. 33 Closeup view of the vortex structure around bow and stern region under different rotation time: (a) to (d) show instantaneous time at t = 5 s, 15 s, 25 s, and 35 s, respectively.

At t=5 s, compared to that at the drift angle of 0°, the bilge vortex tube exhibits a bias towards the port side. By 15 s, 25 s, and 35 s, only the starboard bilge vortex near the bow is evident, with shorter extension distances observed at 25 s and 35 s due to reduced speed. A complex vortex structure forms at the stern of the ship, influenced by interactions and the extrusion of the stern wave system. As the rotation angle changes gradually and speed decreases, the bow's disturbance to the surrounding flow field diminishes, resulting in a corresponding reduction in the vortex structure.

In the rotational movement, the position and intensity of vortex structures continually change with variations in rotational angle, speed, and vortex interactions. Some vortices may strengthen, weaken, or even disappear, affecting the overall distribution of the vortex field.

6. Conclusion

This paper employs the CFD numerical simulation method to explore the flow field characteristics around the bow at the drift angle of 0°, 10°, 20° and manoeuvring (rotary motion). The analysis focuses on the velocity field, pressure distribution, streamline patterns, and vortex structures. The findings lead to the following conclusions:

(1) At the drift angle of 0°, the flow field exhibits symmetric distribution. This symmetrical flow pattern along the hull surface contributes to minimized resistance and enhanced navigation efficiency. Moreover, the symmetry suggests reduced external disturbances on the hull, thereby promoting ship stability during navigation.

(2) During oblique sailing, the flow field exhibits intricate streamlines and vortex structures, deviating from symmetry. This departure from symmetry can lead to increased rolling and hull bumping, which in turn affects navigation stability. Changes in pressure gradients influence the streamline distribution along the hull surface, affecting ship forces and fluid flow paths. This contributes to the bubble sweeping down near the bow. However, the bubble movement is also influenced by various factors, including the velocity field and boundary layer separation.

(3) During manoeuvring with oblique motion (rotary motion), the flow field undergoes dynamic changes across several stages. These stages include straight motion, yawing, significant deceleration, and steady rotation, each reflecting distinct hull motion states. Straight Motion: In this phase, the flow is relatively stable, allowing for predictable behaviour of the hull. Understanding this stage is crucial for assessing baseline performance. Yawing: This stage introduces lateral movement, which disrupts the flow pattern and alters the pressure distribution around the hull. The effects of yawing are significant in terms of manoeuvrability and stability. Significant Deceleration: As the vessel slows down, changes in the flow characteristics can lead to increased drag and potential flow separation. This stage is critical for understanding how the ship responds to rapid changes in speed. Steady Rotation: In this final phase, the flow stabilizes, but the vessel experiences complex interactions between centrifugal forces and fluid dynamics. Analysing this stage helps in evaluating the vessel's performance under sustained turning conditions.

This study elucidates the systematic influence of drift angles on the bow flow field, offering new insights into the flow mechanisms underlying bubble sweep-down during oblique sailing and turning manoeuvres. Nevertheless, certain limitations should be acknowledged: first, the fixed-attitude assumption adopted in the simulations does not account for the effects of ship heel motion; second, the analysis is based primarily on macroscopic flow characteristics without explicit modelling of bubble transport processes. Future work could advance in the following directions: incorporating heel freedom to more realistically represent ship motion responses; employing a coupled Eulerian–Lagrangian approach to directly simulate bubble dynamics; and applying the present findings to engineering practices, such as optimizing the placement of acoustic equipment (e.g., favouring the inside of a turn) and exploring the design of vortex-control appendages at the bow. A thorough understanding of these dynamic flow changes is essential for accurately predicting ship behaviour and for formulating effective navigation strategies.

ACKNOWLEDGMENTS

The research in this paper has been supported by the National Natural Science Foundation of China (grant no. 52471355; 52571375); the Regional Joint Fund of the National Natural Science Foundation of China (grant no. U25A20376); the Natural Science Foundation of Guangdong Province, China (grant no. 2024A1515030042; 2023A1515011720), Southern Marine Science and Engineering Guangdong Laboratory (Zhuhai) (SML2023SP228).

REFERENCES

[1] Phuong, N. H., Taniguchi, T., Katayama, T., 2025. Numerical study of scale effects of viscous roll damping for a container ship. *Brodogradnja*, 76(4), 76406. https://doi.org/10.21278/brod76406

[2] Halder, P., Liu, S., 2025. Numerical investigation of added resistance of a container ship in short regular waves using unsteady RANS simulations. *Brodogradnja*, 76(2), 76204. https://doi.org/10.21278/brod76204

[3] Grlj, C. G., Degiuli, N., Martić, I., 2024. Experimental and numerical assessment of the effect of speed and loading conditions on the nominal wake of a containership. *Brodogradnja*, 75(4), 75405. https://doi.org/10.21278/brod75405

[4] Shao, Y., Song, B., Wang, J., Wang, W., Wan, D., 2025. Wave breaking characteristics around a wedge-shaped bow: High-fidelity simulation of water–air–bubble mixed flow. *Physics of Fluids*, 37(7), 072124. https://doi.org/10.1063/5.0279778

[5] Longo, J., Stern, F., 2002. Effects of drift angle on model ship flow. *Experiments in Fluids*, 32(5), 558-569.

https://doi.org/10.1007/s00348-001-0397-0

[6] Tanaka, S., Kijima, K., 1994. Calculation of cross flow forces acting on a ship at larger drift angles. *Journal of the Society of Naval Architects of Japan*, 176, 251-258. https://doi.org/10.2534/jjasnaoe1968.1994.176_251

[7] Pinto-Heredero, A., Xing, T., Stern, F., 2010. URANS and DES analysis for a Wigley hull at extreme drift angles. *Journal of Marine Science and Technology*, 15, 295-315. https://doi.org/10.1007/s00773-010-0092-z

[8] Bhushan, S., Yoon, H., Stern, F., Guilmineau, E., Visonneau, M., Toxopeus, S. L., et al., 2019. Assessment of computational fluid dynamic for surface combatant 5415 at straight ahead and static drift β = 20 deg. *Journal of Fluids Engineering*, 141(5), 051101. https://doi.org/10.1115/1.4041229

[9] Liu, Y., Yao, J., Xu, F., 2025. RANS investigation on the hydrodynamic performance of a ship moving obliquely in shallow and narrow channel. *Ships and Offshore Structures*, 20(4), 487-504. https://doi.org/10.1080/17445302.2024.2353976

[10] Hosseini, A., Tavakoli, S., Dashtimanesh, A., Mikkola, T., Hirdaris, S., 2024. Drift Test Analysis of a Conventional Planing Hull Utilising CFD and 2D+t Models. *Ocean Engineering*, 308, 118226. https://doi.org/10.1016/j.oceaneng.2024.118226.

[11] Zhang, Y., Windén, B., Ojeda, H. R. D., Hudson, D., Turnock, S., 2024. Influence of drift angle on the propulsive efficiency of a fully appended container ship (KCS) using Computational Fluid Dynamics. *Ocean Engineering*, 292, 116537. https://doi.org/10.1016/j.oceaneng.2023.116537

[12] Okuda, R., Yasukawa, H., Yamashita, T., Matsuda, A., 2023. Maneuvering simulations at large drift angles of a ship with a flapped rudder. *Applied Ocean Research*, 135, 103567. https://doi.org/10.1016/j.apor.2023.103567

[13] Ma, Z., Ji, N., Deng, X., Shi, C., 2024. Influence of scale effect on flow field offset for ships in confined waters. *Brodogradnja*, 75(1), 75106. https://doi.org/10.21278/brod75106

[14] Zhang, S., Liu, J., Li, S., Yasukawa, H., Wu, Q., 2022. Impact of bow shapes on hydrodynamic derivatives due to drifting conditions. *Ocean Engineering*, 245, 110347. https://doi.org/10.1016/j.oceaneng.2021.110347

[15] Wu, D., Wang, J., Wan, D., 2021. Delayed detached eddy simulation method for breaking bow waves of a surface combatant model with different trim angle. *Ocean Engineering*, 242, 110177. https://doi.org/10.1016/j.oceaneng.2021.110177

[16] Capone, A., Pereira, F. A., Maiocchi, A., Di Felice F., 2019. Analysis of the hull wake of a twin-screw ship in steady drift by Borescope Stereo Particle Image Velocimetry. *Applied Ocean Research*, 92, 101914. https://doi.org/10.1016/j.apor.2019.101914

[17] Broglia, R., Zaghi, S., Campana, E. F., Dogan, T., Sadat-Hosseini, H., Stern, F., et al., 2019. Assessment of computational fluid dynamics capabilities for the prediction of three-dimensional separated flows: The Delft 372 catamaran in static drift conditions. *Journal of Fluids Engineering*, 141(9), 091105. https://doi.org/10.1115/1.4042752

[18] Li, J., Martin, J. E., Carrica, P. M., 2019. Large-scale simulation of ship bubbly wake during a maneuver in stratified flow. *Ocean Engineering*, 173, 643-658. https://doi.org/10.1016/j.oceaneng.2019.01.001

[19] Lee, S., Hong, C., 2017. Study on the course stability of very large vessels in shallow water using CFD. *Ocean Engineering*, 145. https://doi.org/10.1016/j.oceaneng.2017.09.064

[20] RoyChoudhury, S., Dash, A. K., Nagarajan, V., Sha, O. P., 2017. CFD simulations of steady drift and yaw motions in deep and shallow water. *Ocean Engineering*, 142, 161-184. https://doi.org/10.1016/j.oceaneng.2017.06.058

[21] Kramer, J. A., Steen, S., Savio, L., 2016. Experimental study of the effect of drift angle on a ship-like foil with varying aspect ratio and bottom edge shape. *Ocean Engineering*, 121, 530-545. https://doi.org/10.1016/j.oceaneng.2016.06.004

[22] Meng, Q., Wan, D., 2016. Numerical simulations of viscous flow around the obliquely towed KVLCC2M model in deep and shallow water. *Journal of Hydrodynamics*, 28(3), 506-518. https://doi.org/10.1016/S1001-6058(16)60655-8

[23] Kim, B., Wang, S., Zhu, Z., Kim, Y., 2023. Numerical simulation of free-running turning test of ship in waves. *Ocean Engineering*, 288, 115951. https://doi.org/10.1016/j.oceaneng.2023.115951.

[24] Abbas, N., Kornev, N., 2016. Study of unsteady loadings on the propeller under steady drift and yaw motion using URANS, hybrid (URANS-LES) and LES methods. *Ship Technology Research*, 63(2), 121-131. https://doi.org/10.1080/09377255.2016.1211582

[25] Fureby, C., Toxopeus, S. L., Johansson, M., Tormalm, M., Petterson, K., 2016. A computational study of the flow around the KVLCC2 model hull at straight ahead conditions and at drift. *Ocean Engineering*, 118, 1-16. https://doi.org/10.1016/j.oceaneng.2016.03.029

[26] Abdel-Maksoud, M., Müller, V., Xing, T., Toxopeus, S., Stern, F., Petterson, K., et al., 2015. Experimental and Numerical Investigations on Flow Characteristics of the KVLCC2 at 30° Drift Angle. *SNAME Maritime Convention*, 3-7 November, Providence, Rhode Island, USA, D021S006R008. https://doi.org/10.5957/WMTC-2015-158

[27] Zhou, M., Roelvink, D., Zou, Z., van Wijhe H. J., 2014. Effects of passing ship with a drift angle on a moored ship. 33rd *International Conference on Offshore Mechanics and Arctic Engineering* (ASME 2014), 8-13 June, San Francisco, California, USA, V08BT06A057. https://doi.org/10.1115/OMAE2014-24515

[28] Xing, T., Bhushan, S., Stern, F., 2012. Vortical and turbulent structures for KVLCC2 at drift angle 0, 12, and 30 degrees. *Ocean Engineering*, 55, 23-43. https://doi.org/10.1016/j.oceaneng.2012.07.026

[29] Kim, S. Y., Kim, Y. G., 2001. Computation of viscous flows around a ship with a drift angle and the effects of stern hull form on the hydrodynamic forces. *Journal of the Society of Naval Architects of Korea*, 38(3), 1-13.

[30] Sundsdal, K. R., Greco, M., Hanssen, F.-C., Lugni, C., 2025. An experimental investigation of drift forces and coupled-motion effects for a 2D ship cross-section in regular waves. *Ocean Engineering*, 341, 122482. https://doi.org/10.1016/j.oceaneng.2025.122482

[31] Söding, H., 2025. Wave drift force and moment in deep and shallow water. *Journal of Marine Science and Engineering*, 13(1), 64. https://doi.org/10.3390/jmse13010064

[32] Zhao, X., Luo, C., Cui, J., Jiang, Y., Chen, X., Li, J., 2025. Numerical study of the bubble wake characteristics for underwater vehicles based on multiscale Euler–Euler method. *Physics of Fluids*, 37(11), 113322. https://doi.org/10.1063/5.0301208

[33] Shao, Y., Song, B., Wan, D., Wang, J., 2025. Numerical study of air entrainment mechanisms and vortical structures in breaking waves. *Ocean Engineering*, 341, 122569. https://doi.org/10.1016/j.oceaneng.2025.122569

[34] Gui, L., Longo, J., Stern, F., 2001. Biases of PIV measurement of turbulent flow and the masked correlation-based interrogation. *Experiments in Fluids*, 30, 27-35. https://doi.org/10.1007/s003480000131

[35] Gui, L., Longo, J., Stern, F., 2001. Towing tank PIV measurement system, data and uncertainty assessment for DTMB Model 5512. *Experiments in Fluids*, 31, 336-346. https://doi.org/10.1007/s003480100293

[36] Larsson, L., Raven, H., 2010. Ship resistance and flow. *Society of Naval Architects and Marine Engineering*, New York, USA.

[37] Hirt, C. W., Nichols, B. D., 1981. Volume of fluid (VOF) method for the dynamics of free boundaries. *Journal of Computational Physics*, 39(1), 201-225. https://doi.org/10.1016/0021-9991(81)90145-5

[38] Muzaferija, S., 1998. Computation of free surface flows using interface-tracking and interface-capturing methods. *Nonlinear Water Wave Interaction*, Computational Mechanics Publications, Southampton, UK.

[39] Kim, J. W., Jang, H., Baquet, A., O'Sullivan, J., Lee, S., Kim, B., et al., 2016. Technical and economic readiness review of CFD-based numerical wave basin for offshore floater design. *Proceedings of the Offshore Technology Conference*, 2-5 May, Houston, Texas, USA. https://doi.org/10.4043/27294-MS

[40] Siemens Digital Industries Software, 2022. Userguide STAR-CCM plus. Versiones 2206. P5609 and 8969.

[41] Li, L., Animasaun, I. L., Koriko, O. K., Muhammad, T., Elnaqeeb, T., 2024. Insight into turbulent Reynolds number at the regular, converging, and diverging outlets: Dynamics of air, water, and kerosene through y-shaped cylindrical copper ducts. *International Communications in Heat and Mass Transfer*, 159, 108044. https://doi.org/10.1016/j.icheatmasstransfer.2024.108044

[42] Wang, F., Animasaun, I. L., Al-Mdallal Qasem, M., Saranya, S., Muhammad, T., 2023. Dynamics through three-inlets of t-shaped ducts: Significance of inlet velocity on transient air and water experiencing cold fronts subject to turbulence. *International Communications in Heat and Mass Transfer*, 148, 107034. https://doi.org/10.1016/j.icheatmasstransfer.2023.107034

[43] Wang, F., Animasaun, I. L., Shamsi, D. M. A., Muhammad, T., Ali, A., 2024. Transient cold-front-water through y-shaped aluminium ducts: nature of turbulence, non-equilibrium thermodynamics, and velocity at the converged and diverged outlets. *Journal of Non-Equilibrium Thermodynamics*, 49(4), 485-512. https://doi.org/10.1515/jnet-2024-0011

[44] Bhushan, S., Yoon, H., Stern., F., Guilmiuau, E., Visonneau, M., Toxopeus, S., et al., 2015. CFD validation for surface combatant 5415 straight ahead and static drift 20 degree conditions. *IIHR—Hydroscience & Engineering*, The University of Iowa, IIHR Technical Report. https://doi.org/10.5957/WMTC-2015-124

[45] Hunt, J.C., Wray, A.A. Moin, P., 1988. Eddies, streams, and convergence zones in turbulent flows. Studying turbulence using numerical simulation databases, 2. Proceedings of the 1988 summer program.